Icarus 241 (2014) 97–113

Contents lists available at ScienceDirect

Icarus

journal homepage: www.elsevier.com/locate/icarus

Intercrater plains on Mercury: Insights into unit definition, characterization, and origin from MESSENGER datasets

Jennifer L. Whitten [a,*], James W. Head [a], Brett W. Denevi [b], Sean C. Solomon [c,d]

[a] Department of Geological Sciences, Brown University, Providence, RI 02912, USA
[b] The Johns Hopkins University Applied Physics Laboratory, Laurel, MD 20723, USA
[c] Department of Terrestrial Magnetism, Carnegie Institution of Washington, Washington, DC 20015, USA
[d] Lamont-Doherty Earth Observatory, Columbia University, Palisades, NY 10964, USA

ARTICLE INFO

Article history:
Received 28 March 2014
Revised 9 June 2014
Accepted 10 June 2014
Available online 19 June 2014

Keywords:
Mercury
Volcanism
Mercury, surface
Geological processes
Cratering

ABSTRACT

Orbital observations by the MErcury Surface, Space ENvironment, GEochemistry, and Ranging (MESSENGER) spacecraft are used to re-evaluate the nature and origin of the oldest mapped plains deposits on Mercury, the intercrater and intermediate plains units defined by Mariner 10 investigators. Despite the large areal extent of these plains, which comprise approximately one-third of the planetary surface area viewed by Mariner 10, their formation mechanism was not well constrained by Mariner 10 imaging. One hypothesis attributed plains formation to ponding of fluidized impact ejecta to create relatively smooth surfaces. Another hypothesis was that these plains are of volcanic origin. To assess the origin of these older plains and the contribution of early volcanism to resurfacing on Mercury, we have used MESSENGER data to analyze the morphology, spectral properties, impact crater statistics, and topography of Mariner 10 type-areas of intercrater and intermediate plains. On the basis of new criteria for the identification of intercrater and intermediate plains derived from these observations, we have remapped 18% of the surface of Mercury. We find that the intercrater plains are a highly textured unit with an abundance of secondary craters, whereas the intermediate plains are composed of both intercrater and smooth plains. We suggest that the term "intermediate plains" not be used to map the surface of Mercury henceforth, but rather this unit should be subdivided into its constituent intercrater and smooth plains units. We argue that a substantial percentage of the intercrater plains are composed of volcanic materials on the basis of (1) examples of areas where ejecta from a small number of superposed craters have transformed smooth plains deposits of volcanic origin into a unit indistinguishable from intercrater plains; (2) the range in ages of intercrater plains deposits as interpreted from crater size–frequency distributions; and (3) the near-global distribution of intercrater plains compared with the uneven distribution of impact basins and their associated ejecta deposits.

1. Introduction

The first spacecraft images of Mercury were obtained by Mariner 10 (M10) during three flybys in 1974–1975. M10 imaged approximately 40% of the planet's surface (Fig. 1), ~55% of which was covered with several different plains deposits. The earliest geological interpretation of images from the first M10 flyby (Murray et al., 1974) included a regional map showing three distinct geologic units: plains material, hilly and lineated terrain, and heavily cratered terrain. The intercrater plains unit shortly thereafter was identified as a subdivision of this "heavily cratered terrain" marked by level to gently rolling, densely cratered surfaces between craters >30 km in diameter (Trask and Guest, 1975; Trask, 1976). From geologic maps (Trask and Guest, 1975; Schaber and McCauley, 1980; DeHon et al., 1981; Guest and Greeley, 1983; McGill and King, 1983; Grolier and Boyce, 1984; Spudis and Prosser, 1984; Trask and Dzurisin, 1984; King and Scott, 1990; Strom et al., 1990) constructed from M10 images, it is clear that the intercrater plains are the most widespread unit on the portion of the planet imaged by that spacecraft. A distinguishing characteristic of the intercrater plains is their high density of small, superposed craters 5–15 km in diameter (Trask and Guest, 1975; Strom, 1977; Leake, 1981) (Fig. 2). According to Trask and Guest (1975), the majority of these small craters are likely to be secondary impact craters formed from material ejected from larger craters

* Corresponding author. Address: Department of Geological Sciences, Brown University, 324 Brook St., Box 1846, Providence, RI 02912, USA. Fax: +1 4018633978.
E-mail address: jennifer_whitten@brown.edu (J.L. Whitten).

http://dx.doi.org/10.1016/j.icarus.2014.06.013
0019-1035/

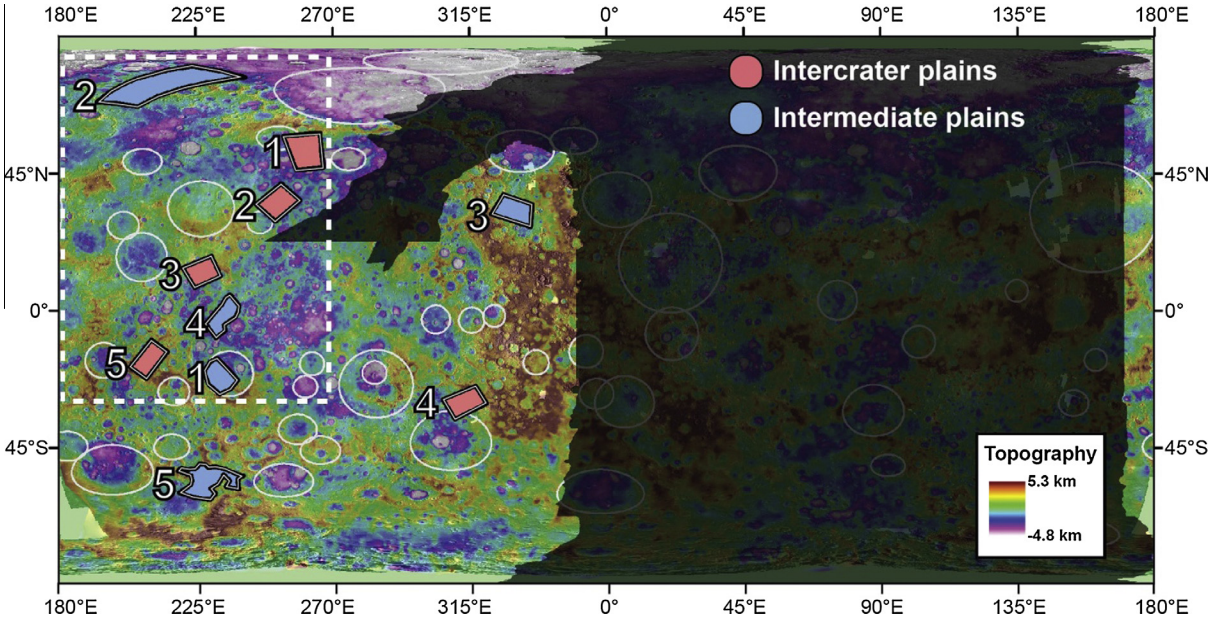

Fig. 1. Map of the study locations in this analysis. Red polygons represent the areas dominated by intercrater plains (ICP), and blue polygons denote the areas dominated by intermediate plains (IP); the numbers are specific identifiers used for reference in the text. The darkened area indicates the part of Mercury that was not imaged by M10. Identified basins (Fassett et al., 2012) are outlined in white. The white dashed box outlines the region mapped in Fig. 8. Overlaid on the MDIS 250 m/pixel mosaic is a model of global topography derived by stereo photogrammetry and referenced to a sphere of radius 2440 km (Edmundson et al., 2011; Becker et al., 2012). Simple cylindrical projection.

(>30 km in diameter) within the heavily cratered terrain. The superposition of these secondary craters was invoked as evidence that the majority of the intercrater plains are older than the heavily cratered terrain (Trask and Guest, 1975). This observed stratigraphic relationship and inferred relative age, combined with the unit extent and crater size–frequency distributions, led to the hypothesis that the intercrater plains are remnants of a volcanic surface that partially predated a period of heavy bombardment of the terrestrial planets (Murray et al., 1975; Trask and Guest, 1975).

The findings from the Apollo 16 mission to the Moon, however, called into question a volcanic origin for plains units on Mercury. Before the Apollo 16 mission, the high-reflectance Cayley plains on which the Apollo 16 astronauts landed were thought to be products of highland volcanism (Milton, 1964; Wilhelms and McCauley, 1971). During the mission (Young et al., 1972) and thereafter (Hodges et al., 1973; Muehlberger et al., 1980), however, the abundance of brecciated material in returned samples (Gast et al., 1973) indicated that these light plains were produced by impact-related processes involving some combination of local, regional, and basin-related material (Eggleton and Schaber, 1972; Head, 1974; Oberbeck et al., 1974). This discovery from the Moon, along with the lack of distinct contrasts in reflectance between surrounding morphologic units on Mercury (Hapke et al., 1975; Rava and Hapke, 1987) and the muted morphology of local wrinkle ridges there (e.g., Strom et al., 1975), prompted some researchers to explore the idea that the intercrater plains on Mercury were emplaced as fluidized ejecta from basin impacts (Wilhelms, 1976; Oberbeck et al., 1977). The surface morphology and reflectance relationships on Mercury matched Cayley plains material more closely than those of the volcanic lunar mare deposits.

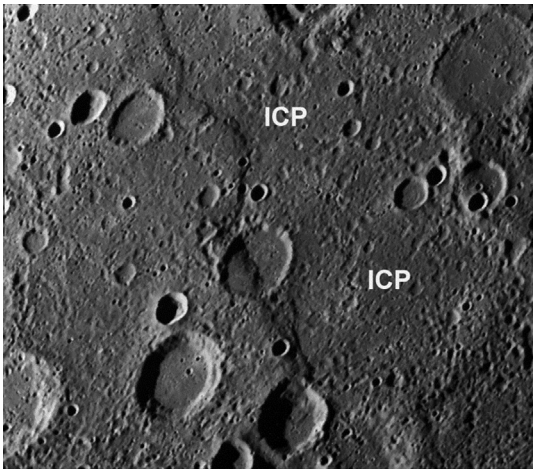

Fig. 2. Example of a Mariner 10 image of intercrater plains (ICP), as defined by Trask and Guest (1975). The lobate scarp Santa Maria Rupes cuts across these intercrater plains from the northwest to southeast. The image is approximately 200 km across; north is up. Mariner 10 frame 27448.

The dominant formation mechanism for the intercrater plains on Mercury continues to be debated, with ideas for the unit's formation focused on two hypotheses: (1) formation as volcanic flows (Murray et al., 1974, 1975; Strom, 1977; Kiefer and Murray, 1987; Spudis and Guest, 1988) and (2) formation by the emplacement of fluidized impact ejecta, an origin similar to that hypothesized for the Cayley plains on the Moon (Trask and Guest, 1975; Wilhelms, 1976; Oberbeck et al., 1977). Another plains unit, the intermediate plains defined in some geological maps constructed from M10 images (Schaber and McCauley, 1980; Guest and Greeley, 1983; McGill and King, 1983; Grolier and Boyce, 1984; Spudis and Prosser, 1984; Trask and Dzurisin, 1984; King and Scott, 1990; Strom et al., 1990), shares many of the same characteristics as the intercrater plains (except that it is less densely cratered), including an uncertain formation origin.

Widespread resurfacing occurred early in Mercury's geologic history, as evidenced by a deficit of craters 20–100 km in diameter compared with the lunar highlands, and at least a portion of that resurfacing is thought to have occurred by the emplacement of intercrater plains (Fassett et al., 2011; Strom et al., 2011; Marchi

et al., 2013). The global distribution of these ancient intercrater plains has a substantial influence on the interpretation of the geologic history of Mercury. If most or all of the intercrater plains are volcanic in origin, then volcanism played a substantial role on Mercury during its earliest history. However, if most of these deposits are impact-related, then a different thermal evolution is implied, perhaps more like that of the Moon, for which the onset of major mare volcanism occurred near the end of the late heavy bombardment of the inner Solar System and partially flooded an earlier crust (Taylor, 1989) of distinctly different composition (e.g., Shearer et al., 2006).

To address these issues, we use observations from the MErcury Surface, Space ENvironment, GEochemistry, and Ranging (MESSENGER) spacecraft, in orbit about Mercury since March 2011, to assess several type areas of intercrater and intermediate plains units defined during geologic mapping from M10 images, and we revisit the interpretations of these areas. In the sections that follow we utilize the high-resolution image and topography data provided by the MESSENGER mission, together with the M10 geologic maps, to define more clearly the intermediate and intercrater plains units in order to understand their origin and role in the geologic history of Mercury and to provide criteria for future mapping. Considerable uncertainty remains regarding the influence and extent of volcanic activity early in Mercury's history, so the confident identification of volcanic units can provide important information about the volcanic flux and thermal history and its relationship to the thermal history of other planetary bodies (e.g., Head and Solomon, 1981). A goal of this analysis is to provide new insights into the definition and distinction of the intercrater and intermediate plains and their origins and to formulate improved guidelines for the definition and use of these unit terms for future analyses with MESSENGER data and in planning for the upcoming BepiColombo mission of the European Space Agency and the Japan Aerospace Exploration Agency (Benkhoff et al., 2010).

2. Methods

To characterize intercrater and intermediate plains, we have examined the M10 geologic unit definitions and used MESSENGER data to reassess and refine these definitions further. Ten different areas located between 0° and 180°E longitude (Fig. 1 and Table 1) and previously mapped with M10 data (Fig. 3, column 4) (Schaber and McCauley, 1980; Guest and Greeley, 1983; McGill and King, 1983; Grolier and Boyce, 1984; Spudis and Prosser, 1984; Trask and Dzurisin, 1984) were chosen for analysis. To facilitate comparison, half of the study regions selected for our reanalysis were originally mapped from M10 images predominantly as intermediate plains, and the other half were mapped predominantly as intercrater plains. These 10 regions were chosen on the basis of the size and continuity of the geologic unit, and all have approximately the same area (~130,000 km^2). For each of the 10 study regions we analyzed images acquired by the MESSENGER Mercury Dual Imaging System (MDIS; Hawkins et al., 2007) and topographic maps and profiles derived from Mercury Laser Altimeter (MLA; Cavanaugh et al., 2007) observations (Fig. 3, columns 1 and 2).

The size–frequency distributions of impact craters were determined for each study region (Fig. 1) to estimate relative ages. MDIS images (Hawkins et al., 2007) were used to identify all visible craters, including embayed craters, greater than ~6 km in diameter (Strom et al., 2008). Including secondary craters in counts can cause a surface to appear older than it actually is because secondary craters on Mercury can have diameters as large as 10 km (e.g., Strom et al., 2008); craters <10 km in diameter were included in this study only if they did not display one of the morphologic characteristics of secondary craters, including an oblate rim, a herringbone pattern, or a location within a chain or cluster. To compare the areal density of impact craters and relative ages of the geologic units, we report values of $N(10)$ and $N(20)$ for each study area, where $N(D)$ is the number of craters with diameter $\geqslant D$ (in km) per 10^6 km^2 area within a given region. The standard deviation (σ) for each value of $N(D)$ is taken to be equal to the square root of the number of craters per diameter bin per area, i.e., $\sigma = [\sqrt{N(D)}/A] \times 10^6$ km^2, where A is the unit area in km^2 (Crater Analysis Techniques Working Group, 1979).

MDIS images have also been used to characterize the morphology of these 10 study areas. Both a 250 m/pixel base map and individual MDIS wide-angle camera (WAC) and narrow-angle camera (NAC) images with resolutions <250 m/pixel were obtained where

Table 1
Locations of areas of intercrater plains and intermediate plains included in this study.

Study regions	Latitude[a]	Longitude[a]	Area (km^2)	Color unit coverage	$N(10)$	$N(20)$
ICP1	52.25	−98.89	1.30×10^5	LRM: 78.5% HRP/IP: 14.1% LBP: 0.02% Unmapped: 7.4%	169 ± 36	62 ± 22
ICP2	35.49	−107.89	1.30×10^5	HRP/IP: 52.9% LRM: 29.2% Unmapped: 17.9%	323 ± 50	162 ± 35
ICP3	12.80	−132.76	1.30×10^5	HRP/IP: 15.2% Unmapped: 84.8%	370 ± 53	162 ± 35
ICP4	−30.09	−46.43	1.30×10^5	HRP/IP: 55.9% Unmapped: 44.1%	300 ± 48	131 ± 32
ICP5	−16.26	−150.51	1.30×10^5	LRM: 15.7% Unmapped: 84.3%	154 ± 34	62 ± 22
IP1	−22.00	−126.85	1.30×10^5	HRP/IP: 59.9% Unmapped: 40.1%	77 ± 24	31 ± 15
IP2	73.77	−148.97	1.30×10^5	Unmapped: 100%	361 ± 53	115 ± 30
IP3	33.00	−30.16	1.30×10^5	HRP/IP: 60.2% Unmapped: 39.8%	223 ± 41	100 ± 28
IP4	−2.17	−126.14	1.30×10^5	HRP/IP: 83.0% Unmapped: 17.0%	177 ± 37	108 ± 29
IP5	−55.86	−130.84	1.30×10^5	Unmapped: 100%	223 ± 41	92 ± 27

[a] Latitude and longitude values are the coordinates for the center of each study region.

available. M10 unit definitions were employed to evaluate the observed morphologies and determine if MESSENGER data support the original unit classification. M10 geologic units were compared with MDIS color image products, such as the global color unit map of Denevi et al. (2009), to determine if there is a correlation between morphologic and color boundaries and also if there are observable color differences within and between the morphologic units. The topography of the intercrater and intermediate plains study regions was characterized with individual MLA profiles, an MLA gridded data product (Zuber et al., 2012), and digital terrain models derived from stereo photogrammetric analysis (Edmundson et al., 2011; Becker et al., 2012) of MDIS images.

3. Results

3.1. Intercrater plains

3.1.1. Morphology

Most of the intercrater plains regions mapped from M10 images have a highly textured surface that appears substantially rougher in the higher-resolution MDIS images (Fig. 3, compare column 1, MESSENGER, and column 5, M10). This surface texture is created by small secondary craters (<10 km in diameter), which are degraded and partially filled with smooth material (Fig. 3a). Larger craters in the study regions are all but completely filled with smooth material, and their rims are almost totally obscured (e.g., Fig. 3a, f and k). Some of these craters would be impossible to identify were it not for the difference in texture between their smooth resurfaced interiors and the highly sculpted crater exterior. Fresh crater chains or secondary clusters are easily identified around younger impact craters, and older crater chains can be identified by the alignment of degraded, filled secondary craters (Fig. 3u). Some study regions have isolated, irregular smooth patches intermixed with the heavily textured surface, and other study regions have parallel lobate scarps (e.g., Strom et al., 1975) that are typically associated with smoother geologic materials (i.e., Fig. 3u).

3.1.2. Topography

Topographic data, generally unavailable from M10, provide important information on the regional elevations of the intercrater plains study areas (Fig. 3, column 2). Three (ICP1, ICP2, and ICP3) of the five intercrater plains study regions are covered by MLA data; for all five study areas there are stereographic data. General agreement between the two topographic datasets in areas of overlap provides confidence that stereo photogrammetry may be used to compare and characterize the intercrater (and intermediate) plains study regions in areas where MLA data are not available. The intercrater plains occur at a variety of elevations, from −0.8 km to 0.5 km relative to a datum of 2440 km radius, according to the average elevation of each intercrater plains study region.

The intercrater plains are more varied in local relief than might be expected for a volcanic plains unit. As shown by Whitten and Head (2013b), heavily cratered terrain on the Moon that has been flooded by volcanic deposits tends to show a narrow range of elevations. In some settings, intercrater plains are seen on highland plateaus and in topographic depressions within close proximity (Fig. 3l). Many of the most abrupt variations in local topography within the intercrater plains are controlled by impact crater ejecta deposits and degraded crater remnants. The modest relief in ICP1 is controlled by large, partially filled impact structures (Chong-Gauguin basin; Fassett et al., 2012), except for the low-lying southern portion of this study area. The 1.0 km elevation change across ICP2 (Fig. 3g) is gradual and is consistent with the lack of any fresh craters >30 km in diameter. In ICP3 the high relief (~1.6 km; Fig. 3l) is produced by the location of the study area on the edge of a plateau east of Budh Planitia, which accounts for the observed increase in topography northward (Fig. 1). There are several depressions formed from older impact structures in the southern portion of ICP3, but they are not part of the intercrater plains. ICP4 is on the western edge of a large, high-standing plateau that extends from 45°N to 45°S and 315°E to 0°E (Fig. 1b), creating ~2.8 km of relief (Fig. 3q) within the study region. The southwestern topographic low is related to an overlap of the "probable" ~830-km-diameter Andal-Coleridge basin (Fassett et al., 2012) with this study region (Fig. 1). ICP5 has a similar geometry; it lies partly on another high-standing plateau to the east–southeast of Tolstoj basin (Fig. 1) and has a relief of ~1.5 km (Fig. 3v); the low-lying topography in ICP5 contains no known major impact structures. The variation in the topography of intercrater plains could be the result of modification by superposed impact craters or changes to long-wavelength topography after plains emplacement (e.g., Zuber et al., 2012; Klimczak et al., 2013).

3.1.3. MDIS color units

Intercrater plains mapped from M10 images are represented in each of the MDIS color units defined by Denevi et al. (2009; Fig. 3, column 3), except for the low-reflectance blue plains (LBP). The majority of ICP3 and ICP5 were not mapped with the flyby MDIS color data owing to poor illumination geometry or lack of coverage. Those regions that do overlap with the MESSENGER MDIS color flyby data are composed of multiple color units, including the high-reflectance red plains (HRP) and intermediate plains (IP), and low-reflectance material (LRM) (Fig. 3, column 3; Table 1), where red and blue denote more and less steeply increasing spectral reflectance from visible to near-infrared wavelengths, respectively. The HRP and IP units were mapped together by Denevi et al. (2009) and are therefore reported together in this paper. Texture differences can be used to distinguish the morphologically smooth HRP/IP unit from the other color units, but there is no consistent textural difference between LRM and geologic materials within other color units. Approximately 50% of both ICP2 and ICP4 are composed of HRP/IP, occurring either as interior material in impact basins and large craters or as a plains-like deposit outside of impact features. The remaining mapped area in ICP2 is composed of ~29% LRM, typically as widespread plains-like units. The remaining area in ICP4 was not mapped by Denevi et al. (2009). ICP1 is mostly composed of LRM material, with minor amounts of HRP/IP. There is no morphologic evidence for flow-like embayments between the different color units in the intercrater plains.

3.1.4. Crater statistics

Cumulative crater size–frequency distributions (SFDs) were computed for each of the five intercrater plains study regions (Fig. 4a–e). The superposed craters range in size from 6 km in diameter to several hundred kilometers in diameter. For most of the ICP study regions, the SFDs have a similar slope and density of impact craters, especially those <30 km in diameter, except for ICP1 and ICP5 (see below). Collectively, the crater SFDs for intercrater plains overlap and have a slightly higher crater density at a given diameter than intermediate plains study regions (Fig. 4k).

As expected for Mercury, the steep slopes of the crater SFDs at diameters <10 km (Fig. 4a, e, f, i and j) are believed to be the result of secondary cratering (Strom et al., 2008; Xiao et al., 2014), an interpretation supported by the abundant secondary craters visible (Fig. 3, left column). Several of the crater SFDs have a steep roll-off for the bins at the largest crater diameters (ICP2, ICP4 and ICP5; Fig. 4b, d and e), consistent with the finding of others that Mercury is deficient in craters 20–100 km diameter relative to the Moon (Fassett et al., 2011). ICP1 has a lower density of craters 12–20 km diameter, a result that could be a consequence of

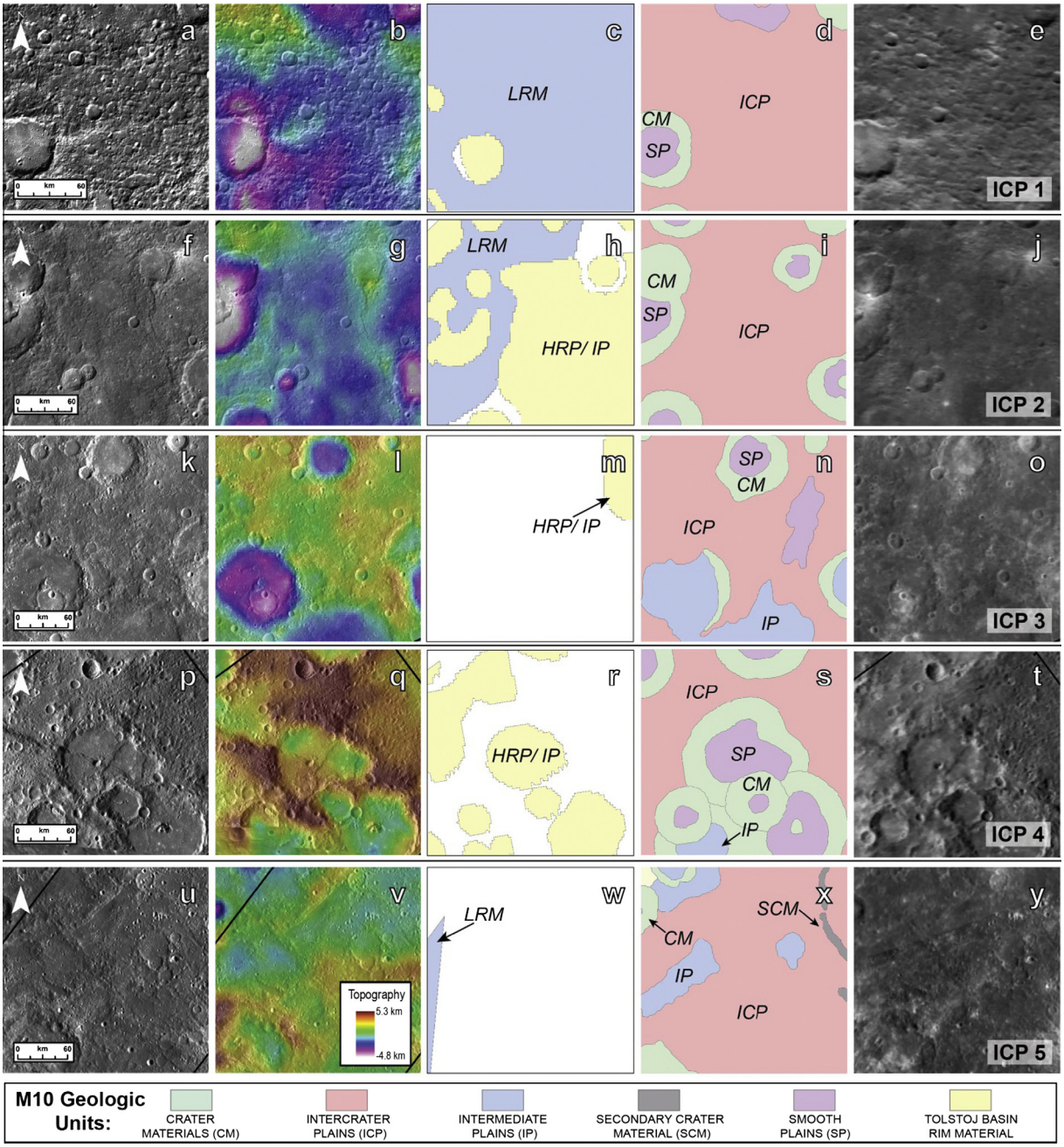

Fig. 3. Subsets of the intercrater plains (ICP) study regions identified in Fig. 1. Column 1: MDIS 250 m/pixel mosaic or WAC and NAC images. North is up (white arrow). Column 2: topography data from stereo photogrammetry (~2.6 km/pixel) overlaid on MDIS data. Column 3: color units mapped by Denevi et al. (2009). White areas are unmapped. Column 4: M10 geologic map. Column 5: M10 images. (a) is from images EW0226880104G, EW0226837761G and EW0226795417G. (f) is from images EW0226964416G, EW0226922188G, and EW0226879730G. (k, p, and u) are from the 250 m/pixel MDIS base map. All images and maps are in stereographic projections centered on the given study region (see Table 1 for coordinates).

resurfacing from Chong-Gauguin basin (~330 km in diameter), located in the northwest corner of the study region. The $N(10)$ values for the intercrater plains study regions vary between 154 ± 34 and 370 ± 53, and $N(20)$ values are between 62 ± 22 and 162 ± 35 (Table 1). These ranges correspond to Tolstojan to pre-Tolstojan ages (Fig. 5; Spudis and Guest, 1988).

The intercrater plains study regions were analyzed for spatial relationships between the locations of small secondary craters and the proximity of fresh impact craters. Nearby fresh impact craters could cause intercrater plains regions to be artificially aged by an abundance of secondary craters. To assess this possibility, the relationship between crater diameter and maximum distance of secondary craters (Gault et al., 1975) was extrapolated linearly to determine the maximum distance of secondary craters for 23 fresh impact craters adjacent to our study regions. We found no relationship between proximity of relatively fresh impact craters and the steepness of the upturn observed in the crater SFDs. Such a lack of a relationship is in part a result of our attempt to exclude secondary craters from the crater counts; fresh secondary craters are much easier to identify and exclude from crater counts than degraded ones. Thus, the upturns observed in SFDs likely result from the inclusion of morphologically degraded secondary craters which, at this size range, are difficult to distinguish from degraded primary craters.

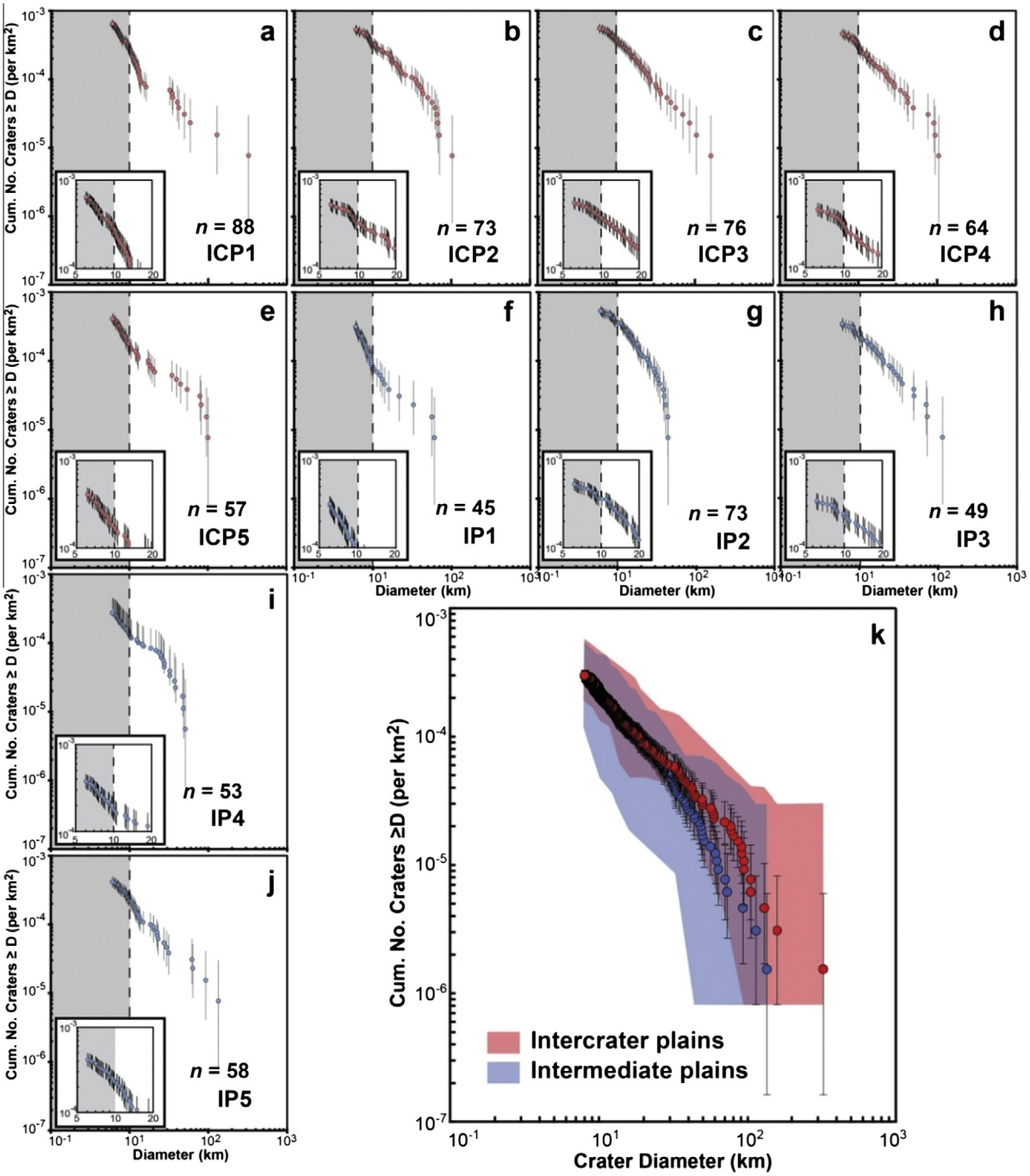

Fig. 4. (a–j) Cumulative crater size–frequency distributions for the intercrater and intermediate plains study regions. Insets are expanded views of the size–frequency distributions for craters between 5 and 20 km diameter. Gray regions indicate portions of the crater size–frequency distribution strongly affected by secondary craters, as evidenced by the break in slope near 10 km diameter (dashed line). For several study regions, this break in slope is less obvious because we attempted to avoid secondary craters in constructing these plots. Nonetheless, it is clear that avoiding secondary craters in this size range is difficult for Mercury and poses a challenge for determining crater size–frequency distributions at smaller diameters (Strom et al., 2008). Some of the distributions have shallow slopes at the smallest diameters because not all of these smallest craters (~6 km diameter) were counted. The number *n* of craters counted in each study region is indicated. (k) Average crater size–frequency distributions for the intercrater and intermediate plains study regions and their associated errors. Red and blue areas span the range of values for individual study areas.

3.1.5. Intercrater plains: Summary

To summarize, intercrater plains are densely cratered at diameters <10 km in diameter, and this extensive cratering has created a highly textured surface. Despite the surface roughness, several broad morphologic features that might be the result of volcanism are distinguishable, such as large infilled craters (e.g., Fig. 3a, k and u), but no specific volcanic features (e.g., vents, flow fronts) were identified. The resolution of the MESSENGER dataset enabled the identification of these characteristic features, which are useful criteria for further mapping of intercrater plains and provide a sharper view of the surface than did M10 data (Fig. 3, column 5). The intercrater plains as defined and mapped do not have any clear relation with topography (Fig. 3, column 2). This unit covers high-standing plateaus and continues into topographic depressions. The

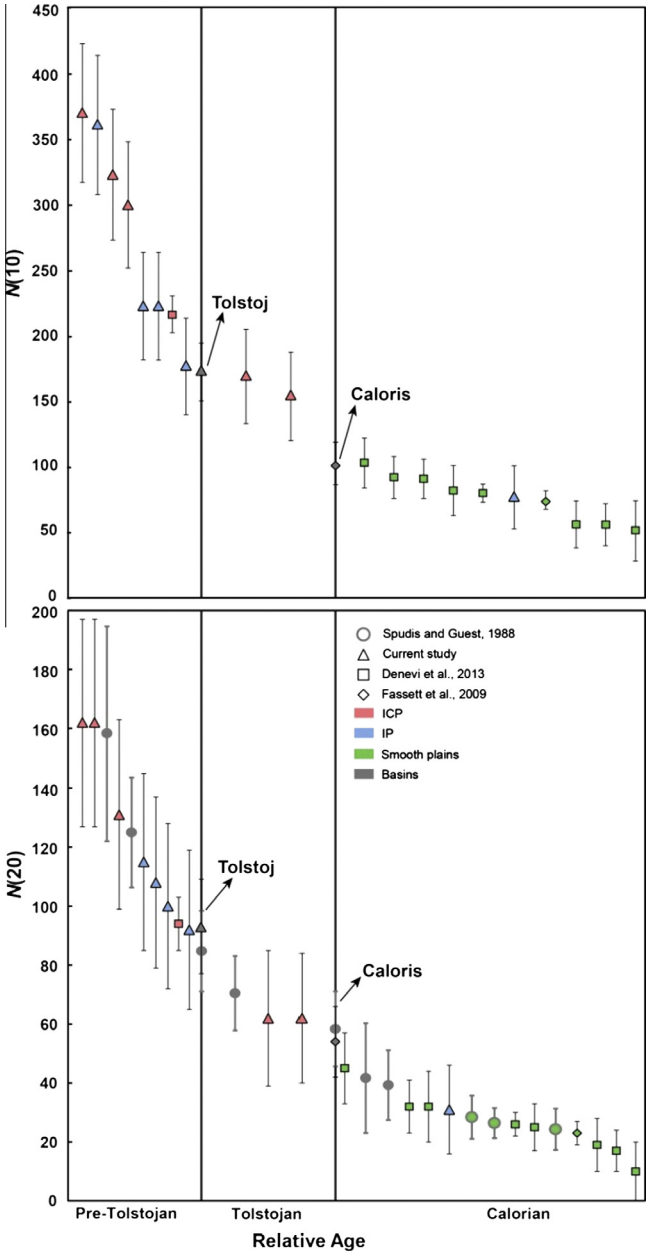

Fig. 5. Crater density values $N(10)$ (top) and $N(20)$ (bottom) for the ICP and IP study regions of this paper, as well as for different plains areas (Spudis and Guest, 1988; Denevi et al., 2013a) and basins (Spudis and Guest, 1988; Fassett et al., 2009) on Mercury. The plots show that $N(10)$ and $N(20)$ values provide consistent estimates of relative age. Values for intercrater and intermediate plains indicate that these units are Tolstojan to pre-Tolstojan in age. Errors in N are large for several study regions, which implies that many of the study areas could have formed at any time during the pre-Tolstojan and Tolstojan periods. Spudis and Guest (1988) did not report $N(10)$ values. The figure is modeled from Fig. 26 of Spudis and Guest (1988), so the abscissa is aligned with corresponding lunar stratigraphic systems (Pre-Nectarian, Nectarian, and Imbrian periods), for which absolute ages are known or may be estimated. Data points are arbitrarily spaced evenly within each time period.

intercrater deposits identified from M10 images are not composed of a single color unit (Denevi et al., 2009). Different regions of the intercrater plains have some of the reddest (HRP/IP) and bluest (LRM) spectral reflectance, as well as the highest (HRP/IP) and lowest (LRM) reflectance values, suggesting that whatever their origin(s), the intercrater plains have a range of color unit variations. We confirm the pre-Tolstojan and Tolstojan age estimates of these intercrater plains regions (Fig. 5).

3.2. Intermediate plains

3.2.1. Morphology

Most of the intermediate plains regions are composed of many moderately cratered smooth plains-like deposits (Fig. 6a, k and p) with some highly textured regions (Fig. 6f and u). The highly textured surfaces result from a combination of sculpted ejecta and small secondary craters and appear similar to the intercrater plains. Recent crater chains (Fig. 6a) and, in a few study regions, parallel lobate ridges (Fig. 6k) are observed. In the smoother regions there is evidence for buried craters (typically <25 km diameter), such as partially buried rims and wrinkle-ridge rings (Fig. 6p). Such circular patterns of wrinkle ridges are believed to have been formed by compressional stresses localized by a shallowly buried crater rim crest (Guest and Fielder, 1968; Cruikshank et al., 1973; Watters, 1993; Freed et al., 2012; Watters et al., 2012) and are typically observed in volcanic terrains (e.g., Lambert R on the Moon and Mercury's northern smooth plains; Head et al., 2011). Impact-degraded craters are identified by filled interiors and disrupted crater rims that have been modified by ejecta from later impact events. A lunar example of an impact-modified crater is the Ptolemaeus crater, which was filled with Imbrium ejecta and had its rim scoured by Imbrium ejecta. Larger craters in intermediate plains are partially infilled (e.g., Fig. 6f and u), and the more degraded craters have lost most of their rim elevation.

3.2.2. Topography

IP1 is located within the Beethoven basin, and its surface slopes down toward the center of the basin (Fig. 6b). IP2 (Fig. 1) has a ridge through its center and slopes toward the northern smooth plains and Suisei Planitia to the south (total relief is ~2.0 km). Stereographic data show that IP3 (Fig. 1) has a large north–south-trending trough (~175 km wide) with a total relief of ~1.2 km in the study area. The topography in IP4 (Fig. 6q) is generally low-lying, partially the result of an unnamed ~245-km-diameter crater in the northern part of the study region (Fig. 1). IP5 (Fig. 6v) is located within a heavily cratered region containing highly undulating crater topography (i.e., crater rims and depressions). MLA and stereographic data indicate that the morphologically smooth regions of the intermediate plains are located at lower elevations than the rougher textured material (intercrater plains). Similar to the case for intercrater plains, much of the observed topographic variability of intermediate plains could be the result of impact crater morphology (fresh or degraded) or changes to long-wavelength topography subsequent to plains emplacement (e.g., Zuber et al., 2012; Klimczak et al., 2013).

3.2.3. MDIS color units

Several of the selected intermediate plains study regions were mapped using the MESSENGER flyby color data (Denevi et al., 2009), including IP1, IP3, and IP4. IP2 and IP5 were not mapped owing to poor viewing conditions (Fig. 6, column 3; Table 1). The three regions of intermediate plains mapped are >50% HRP/IP, and the remaining area was unmapped. In contrast to the M10 intercrater plains, which are characterized by a wide variety of color units, the intermediate plains appear to have generally similar MDIS color characteristics; the unit is dominated by HRP/IP material. This HRP/IP color signature has also been correlated with the presence of smooth plains units identified by their morphology and interpreted to be of volcanic origin (e.g., Robinson et al., 2008; Denevi et al., 2009; Head et al., 2011). The agreement in MDIS color characteristics between the M10-defined intermediate plains and M10- and MESSENGER-defined smooth plains material is consistent with the observation of many small patches of smooth plains

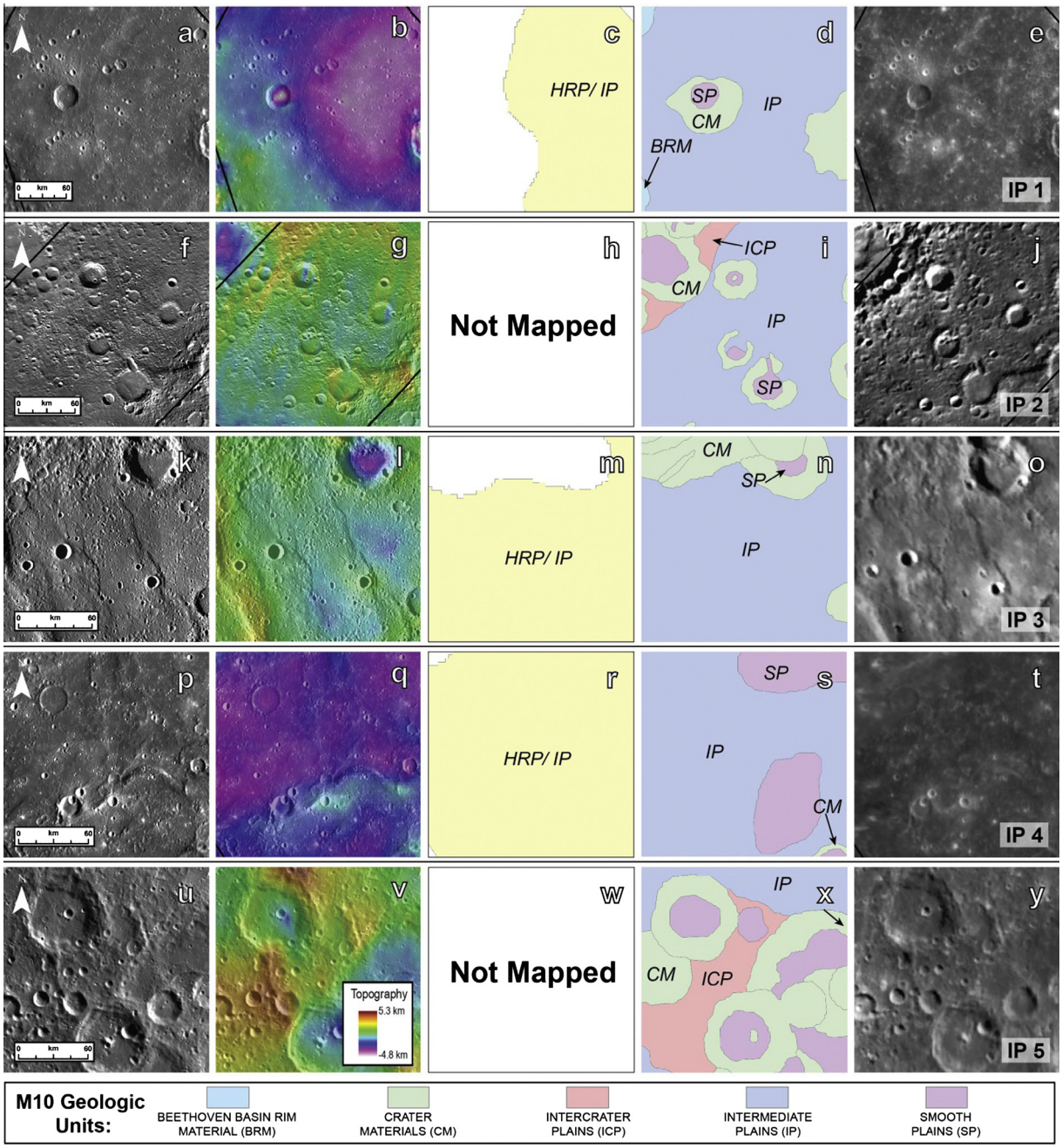

Fig. 6. Subsets of the intermediate plains (IP) study regions identified in Fig. 1. Column 1: MDIS 250 m/pixel mosaic or WAC and NAC images. North is up (white arrow). Column 2: topography data from stereo photogrammetry (~2.6 km/pixel) overlaid on MDIS data. Column 3: color units mapped by Denevi et al. (2009). White color indicates unmapped region. Column 4: M10 geologic map. Column 5: M10 images. (a) is from the 250 m/pixel MDIS base map. (f) is from images EW0214589955G, EW0214589935G, EW0214676881G, and EW0214633400G. (k) is from images EW0213025967G, and EW0213025938. (p) is from images EN0226963098M, EN0226920771M, EN0226920672M, and EN0226920674M. (u) is from image EN0227550741M. All images and maps are in stereographic projections centered on the given study region (see Table 1 for coordinates).

deposits within the M10-mapped intermediate plains (Fig. 6, column 1).

3.2.4. Crater statistics

As is the case with the intercrater plains, the intermediate plains study regions have an abundance of secondary craters, as indicated by the sharp upturn in crater SFDs at diameters <10 km (Fig. 4f–j). In IP2 and IP3 there is a small break in slope at 10 km before the crater SFD levels out at the smallest crater diameters, likely due to incomplete counting in the smallest-diameter bins. Most of these crater SFDs cluster together on a cumulative plot (Fig. 4k). IP1 (Fig. 4f) is an outlier crater SFD, having a different shape to its distribution and a lower overall density of craters at all sizes. IP2 and IP3 are almost uniformly cratered across their surfaces and show a crater SFD more typical for intermediate plains (Fig. 4g and h). IP4 and IP5 show distributions (Fig. 4i and j) potentially indicative of resurfacing, an inference supported by embayed and partially buried craters in IP4 (Fig. 6p). The $N(10)$ values for the intermediate plains study regions have a larger range, from 77 ± 24 to 361 ± 53, than the intercrater plains study regions (Table 1). Calculated $N(20)$ values are between 31 ± 15 and 115 ± 30 and correspond to Calorian through pre-Tolstojan ages (Spudis and Guest,

1988). From the $N(20)$ values, IP1 is associated with the Calorian time period, along with many other smooth plains deposits (Spudis and Guest, 1988). The $N(10)$ and $N(20)$ values for the four remaining intermediate plains regions correspond to the pre-Tolstojan time period (Fig. 5).

3.2.5. Intermediate plains: Summary

On the basis of high-resolution MESSENGER datasets, the intermediate plains unit defined at M10 resolution appears in the study regions examined here to be a combination of older intercrater plains units and younger smooth plains deposits, rather than a distinctive geologic unit. Fresh crater chains, lobate scarps, and buried craters are observed in this map unit (Fig. 6k). No volcanic landforms (e.g., vents, flow fronts) were detected within the unit. Many of the smooth plains associated with the M10-mapped intermediate plains are topographically lower than some of the other more heavily cratered parts (i.e., IP5; Fig. 6u and v). With the exception of IP1, all of these intermediate plains regions have crater size–frequency distributions that overlap with those for the intercrater plains (Fig. 4k) and correspond to the pre-Tolstojan time period (Fig. 5; Table 1).

4. Discussion

4.1. Summary of intercrater and intermediate plains units

The intercrater and intermediate plains units require more stringent identification criteria than were used previously in order to avoid confusion. M10 mapping efforts indicated that the intercrater plains covered a third of the imaged surface of Mercury (e.g., Strom, 1977; Kiefer and Murray, 1987), and MESSENGER data support the conclusion of widespread intercrater plains deposits. Comparisons of the MESSENGER and M10 image data (Fig. 3) show that the higher resolution and variety of the MESSENGER datasets have enabled a more detailed definition and analysis of the intercrater plains. However, in contrast to areas of smooth plains (Denevi et al., 2013a), the new MESSENGER data reveal no specific color or topographic characterization for intercrater plains that might permit distinction from surrounding units similarly older than smooth plains. MDIS color data show that the intercrater plains have variable color characteristics; all but the LBP color unit of Denevi et al. (2009) can be found in intercrater plains areas. There is no evident relation between topography and the distribution of intercrater plains; intercrater plains can be found in topographic lows, atop the highest plateaus on Mercury, and at elevations and slopes in between. According to our analysis of MESSENGER data, in support of the findings of M10 mappers, the intercrater plains can be most readily distinguished by a more densely cratered surface than that of the smooth plains (Fig. 3, column 1) and crater density values corresponding to the Tolstojan to pre-Tolstojan periods.

A comparison of MESSENGER (Fig. 6, column 1) and M10 (Fig. 6, column 5) images shows why ambiguity over the definition of the intermediate plains persisted. The lower resolution and illumination geometries of M10 data "smoothes away" some of the texture created by secondary impact craters (Fig. 6k, o, p and t), confusing unit identification. Our analysis indicates that intermediate plains mapped from M10 images are a combination of highly textured material and small pockets of smooth plains material (Fig. 6, column 1). The intermediate plains are composed primarily of the HRP/IP MDIS color unit, and in several study regions (i.e., IP3) the HRP/IP unit corresponds to the location of low-lying smooth plains

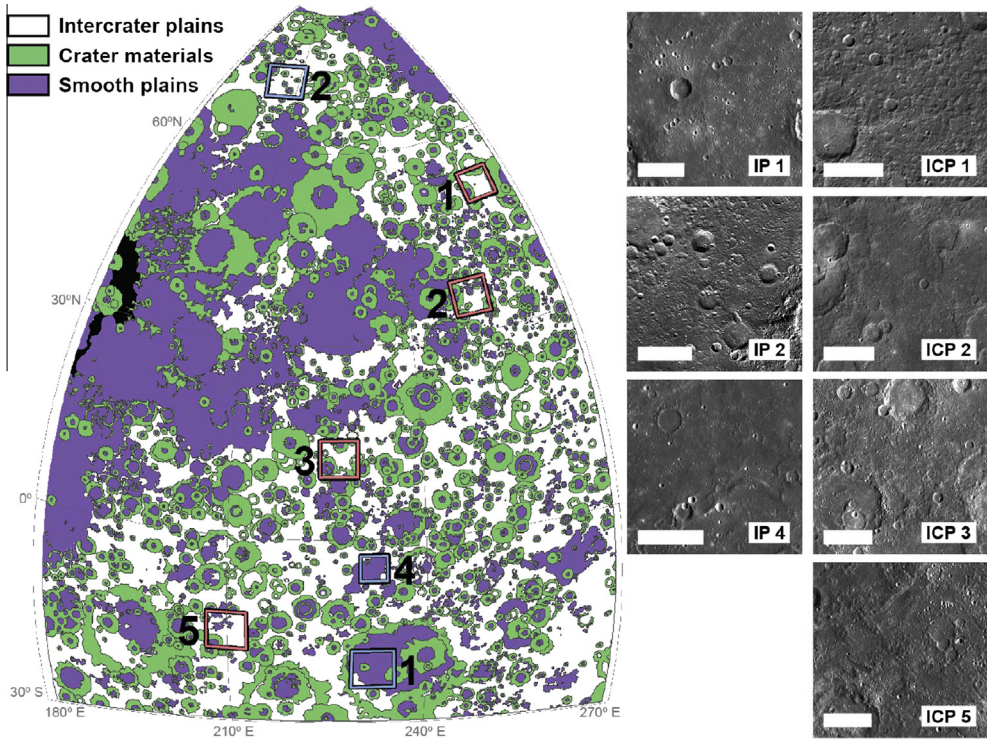

Fig. 7. Geologic map constructed with the unit identification criteria developed in this study. The region shown is located to the east of the Caloris impact basin (Fig. 1); many of the smooth plains in the western portion of this region are circum-Caloris deposits. An MDIS close-up image of each study region (column 1, Figs. 3 and 6) is included to the right of the sketch map; north is up in each image, and all scale bars (white) are 60 km in length. The MDIS images are in stereographic projections centered on the given study region. The locations of these images on the map are indicated by red (intercrater plains, labeled by number to the left of the boxes) and blue (intermediate plains, labeled by number to the right of the boxes) outline. Caloris interior deposits that were not mapped into one of the three units defined in this study are shown in black. The geologic map is in a Lambert azimuthal equal-area projection centered on the map region.

deposits. In addition, the M10 intermediate plains map unit has an abundance of secondary craters <10 km in diameter (i.e., upturn at 10 km; Fig. 4), sharing this defining quality of the intercrater plains. The majority of the M10 intermediate plains are dated as pre-Tolstojan (Fig. 5) on the basis of crater density values, suggesting that these deposits formed early in the geologic history of Mercury.

On the basis of this analysis, we propose that the definition of intercrater plains should include a highly textured surface morphology (Fig. 3a, f, k and p) with few smooth patches. The units we mapped had a high crater density, $N(10)>\sim225$, and an upturn in their crater SFDs at diameters <10 km that is attributed to an abundance of secondary craters. Intermediate plains should be analyzed in detail and subdivided into either intercrater or smooth plains units; the highly textured regions with the abundance of secondary craters (as indicated by the upturn in the crater SFDs, Fig. 4) should be included in the intercrater plains unit, and patches of smooth plains material >750 km^2 (partially infilling craters ~50 km in diameter or greater) should be grouped with other smooth plains deposits. These proposed geologic unit definitions require the reclassification of several study regions, as described below.

IP1 is located in the center of Beethoven basin (Figs. 1, 6 and 8), and on the basis of morphology, MDIS color, and crater size–frequency distribution it should be reclassified as smooth plains material (Denevi et al., 2013a). The $N(20)$ value of 31 ± 15 for IP1 is comparable to smooth plains $N(20)$ values, which range from 10 ± 10 to 45 ± 12 (Fig. 5; Table 1; Denevi et al., 2013a). Other intermediate plains regions, including IP3 and IP4 (Figs. 1, 6 and 8), should also be reclassified as smooth plains. The morphology of these two study regions is smooth with some small regions having a more intercrater-plains-like texture, again with smoother areas located at lower elevations. Low $N(10)$ values, corresponding to a lower density of secondary craters, for IP3 and IP4 are closer to smooth plains values than to intercrater plains $N(10)$ values (Table 1). The low $N(10)$ value is in contrast to the higher $N(20)$ values, suggestive of a pre-Tolstojan age. This apparent contradiction in crater density values may indicate an extended interval of volcanic eruptions, as detailed below (Section 4.4). The prevalence of the HRP/IP MDIS color unit (Denevi et al., 2009) in these two regions, coupled with the latest mapping of smooth plains deposits (Denevi et al., 2013a), supports such a reclassification of IP3 and IP4. IP5 (Figs. 1, 6 and 8) shows the same general characteristics as IP3 and IP4. The morphology of the unit indicates that IP5 is likely to be an older smooth plains deposit. IP2, in contrast, should be mapped as intercrater plains, on the basis of its heavily cratered texture (Fig. 6, column 1) and intercrater plains-like crater size–frequency distribution (Table 1). The $N(10)$ and $N(20)$ values for IP2 are among the highest values for all of the study areas.

In addition to the reclassification of intermediate plains, there is one intercrater plains study region (ICP5) that, according to our interpretation of the $N(10)$ crater density values (Table 1), should be labeled as smooth plains. However, the interpretation as smooth plains is not supported by the morphology of the study area. ICP5, located to the east of Tolstoj basin (Fig. 1), includes regions of smooth plains that embay older intercrater plains deposits. This interpretation of the local stratigraphy is supported by the topography data, with smooth plains located in low-lying areas and the older intercrater plains areas having higher elevations (Fig. 3v). The surface of ICP5 is covered with ancient northwest–southeast-trending secondary crater chains from Valmiki crater (~210 km diameter) and younger secondary craters from Sophocles crater (~142 km diameter). The calculated $N(10)$ value of 154 ± 34 is consistent with other smooth plains values, as is the $N(20)$ of 62 ± 22 (Table 1). It appears as though the recent secondary impact modification has roughened the surface sufficiently

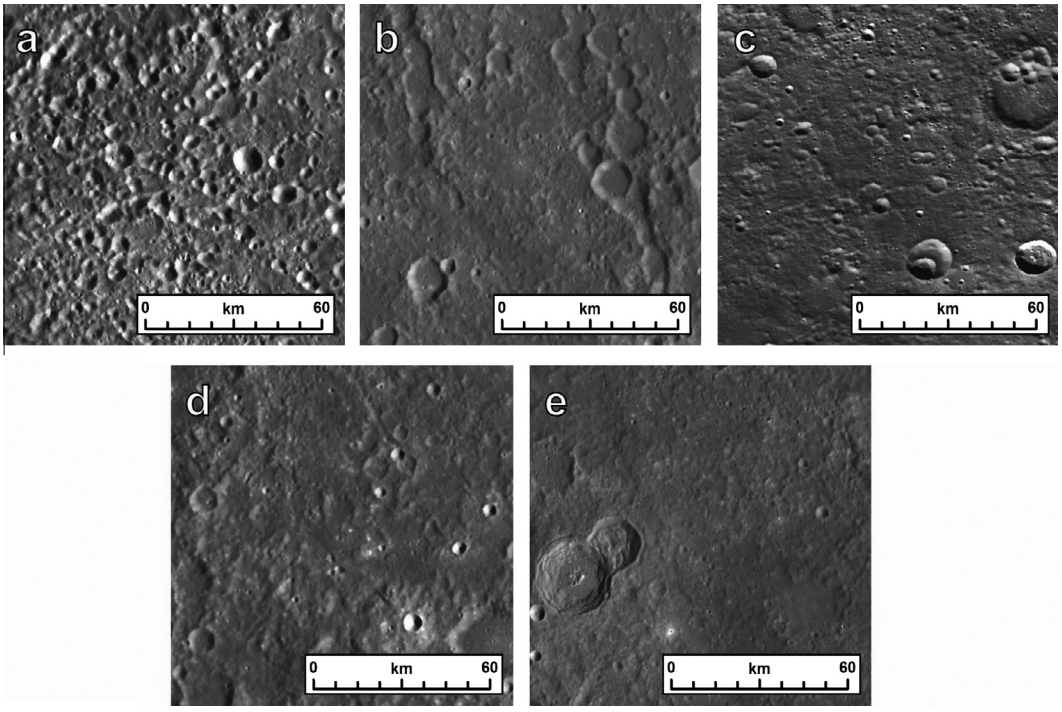

Fig. 8. Examples of the different morphologies included in the intercrater plains map unit. (a) Superposed secondary craters from relatively immature impacts. Secondary craters have sharp and easily identifiable crater rims and can occur in chains. (b) Older secondary craters and chains with flat floors. Some crater rims blend in with the background hummocky texture. (c and d) Mixtures of degraded and fresh craters. In (c) there are more fresh craters and degraded craters are more easily distinguishable. In (d) the degraded craters are difficult to identify individually and thus contribute more to forming a hummocky textured surface. (e) Areas with no obvious secondary craters or chains. Superposed secondary craters are indistinguishable from one another and blend together to form a hummocky texture. All images are from the MDIS 250 m/pixel base map. Lambert azimuthal equal-area projection, centered on the map region in Fig. 7.

to characterize ICP5 as intercrater plains; the conflict between the morphologic interpretation and the $N(10)$ and $N(20)$ values that are similar to those of smooth plains deposits indicate that, in this particular location, secondary crater production has outpaced that of primary impacts.

4.2. Discussion of criteria to distinguish intercrater plains formation processes

As noted above, two hypotheses have been proposed to explain the formation mechanism for intercrater plains, volcanism (Murray et al., 1974, 1975; Strom, 1977; Kiefer and Murray, 1987; Spudis and Guest, 1988) and emplacement as fluidized ejecta from large impacts (Wilhelms, 1976; Oberbeck et al., 1977). Here we discuss the identification criteria (Table 2) that may be useful in distinguishing between these hypotheses for specific intercrater plains deposits.

The Mariner 10 science team interpreted the intercrater plains to be mostly volcanic deposits, on the basis of the extensive areal distribution of the deposits (e.g., Murray et al., 1975) as a major piece of evidence. Mapped intercrater plains deposits are widespread across the surface of Mercury (Trask and Guest, 1975; Schaber and McCauley, 1980; Guest and Greeley, 1983; McGill and King, 1983; Grolier and Boyce, 1984; Spudis and Prosser, 1984; Trask and Dzurisin, 1984; King and Scott, 1990; Strom et al., 1990), implying that the formation process was active on essentially a global scale. The extended distribution of volcanic smooth plains, especially the northern smooth plains and Caloris (Fassett et al., 2009; Head et al., 2011; Denevi et al., 2013a), coupled with models of magma ascent and eruption (Wilson and Head, 2008), suggests that flood basalt volcanism was the dominant eruption style for smooth plains on Mercury and may have been for intercrater plains as well.

Additionally, M10 data and the acquired MDIS global coverage of Mercury have revealed a deficit of craters 20–100 km in diameter compared with the Moon (e.g., Strom, 1977; Strom et al., 2008; Fassett et al., 2011), interpreted to be the result of volcanic plains formation during the period of heavy bombardment of the inner Solar System. Basins >300 km in diameter on Mercury have an asymmetric distribution, with the majority of large basins occurring in the western hemisphere (Fassett et al., 2012). This asymmetric distribution of basins implies an asymmetric distribution of remaining impact basin deposits and thus could indicate that older basins have been modified beyond recognition by volcanism instead of later impact events.

Volcanic deposits might be expected to have distinct compositional boundaries coincident with morphologic boundaries, in a manner similar to the smooth plains deposits (Robinson and Lucey, 1997; Robinson et al., 2008; Denevi et al., 2009, 2013a). Volcanic deposits might also contain volcanic vents or other diagnostic landforms (e.g., Head et al., 2009a, 2009b; Byrne et al., 2013; Hurwitz et al., 2013).

MESSENGER Gamma-Ray Spectrometer (GRS) measurements of the surface abundances of the radioactive elements Th, K, and U indicate that Mercury's interior heat production may have been four times higher ~4 Ga than at present (Peplowski et al., 2011). Such greater heat production could have supported partial melting of the mantle and widespread source regions for volcanic activity during the period of heavy bombardment. Additionally, the lack of a low-density anorthositic crust and the low abundances of iron and titanium in volcanic materials on Mercury (Nittler et al., 2011) may have prevented the generation of magmas higher in density than average crustal material, in contrast to the situation on the Moon (e.g., Head and Wilson, 1992) and favorable to early surface eruptions.

Under the fluidized ejecta hypothesis, impact melt or impact ejecta and locally excavated material ponded in topographic lows and produced plains that were later covered with myriad secondary craters. Instead of forming large continuous deposits, such material was more likely to form discrete smaller deposits similar to the Imbrian smooth plains (Wilhelms and McCauley, 1971; Oberbeck et al., 1977; Meyer et al., 2013) that are concentrated in isolated patches around the lunar nearside basins. Regional heterogeneity in the color properties of intercrater plains might be expected if the unit were produced from impact-related processes, depending on the lateral and vertical heterogeneity of Mercury's crust (Denevi et al., 2009) and the depth of excavation of individual impacts. On the other hand, lunar light plains do not show major variations in color properties relative to background highlands; exceptions are subtle differences related to cryptomaria (e.g., Hawke and Spudis, 1980; Antonenko et al., 1995; Whitten and Head, 2013a). The heterogeneous MDIS color properties of intercrater plains could also result from mixing of crustal materials by the ~4 Gy of impacts after plains emplacement.

Cratering models for the terrestrial planets (e.g., Richardson, 2009) suggest that the lunar highlands are saturated (meaning that for each new crater formed another crater of similar diameter is

Table 2
Lines of evidence that would support a volcanic or impact origin for the intercrater plains.

	Volcanic		Impact
1.	Widespread distribution	1.	Smaller discrete deposits associated with craters or basins
2.	Continuous, areally extensive deposits (~10^5 to 10^6 km^2)[a]	2.	Concentration around large basins and craters
3.	Paucity of craters <100 km in diameter[b]	3.	Spectral characteristics similar to those of surrounding terrain
4.	Spatial density and distribution of large basins (>500 km diameter)[c]	4.	Proportionally more melt in craters on Mercury than the Moon[d]
5.	Distinct compositional boundaries within or at margins of deposits[e]	5.	Abundance of primary craters, coupled with cratering models indicating surface saturation for craters >128 km in diameter[f]
6.	Specific landforms (e.g., ghost craters, sinuous rilles, rimless depressions, wrinkle ridges)[g]		
7.	Interior heat production and thermal history[h]		

[a] Head et al. (2011) and Denevi et al. (2013b).
[b] e.g., Strom (1977), Strom et al. (2011) and Fassett et al. (2011).
[c] Fassett et al. (2012).
[d] e.g., O'Keefe and Ahrens (1977) and Cintala (1992).
[e] Robinson et al. (2008) and Denevi et al. (2009).
[f] Richardson (2009).
[g] e.g., Head et al. (2008, 2009a, 2009b).
[h] Peplowski et al. (2011).

destroyed). Mercury (Fassett et al., 2011) shows a size distribution of large craters (>128 km in diameter) similar to that of the Moon, providing support for an impact-related origin for some intercrater plains deposits. Regardless of the dominant formation process, the intercrater plains have been extensively modified by primary and secondary impact cratering.

4.3. Geologic mapping

Analysis of the plains units identified in the M10 geologic maps with MESSENGER data suggests that surface morphology provides good criteria for the definition and identification of smooth plains, but poor criteria for the intercrater plains (i.e., the lack of color contrasts and extensive topographic variation) other than high values of crater density. A regional assessment and a remapping of these major units were completed over a broad study region spanning 18% of the surface of Mercury; the resulting map is shown in Fig. 7. This remapping exercise provides a basis for assessing the candidate modes of origin for intercrater and intermediate plains.

4.3.1. Definition of map units

4.3.1.1. Crater materials. Crater rims, central peaks, and ejecta deposits were mapped for all observable craters > 20 km in diameter. Buried craters were not mapped because their original morphology has been obscured by plains deposits. Digital terrain models from stereo photogrammetry and MDIS image data were used to determine the extent of crater ejecta deposits. Only the continuous ejecta deposit was mapped for most craters because its morphology is more readily distinguished for each individual crater. Determining the extent of the secondary crater field for individual impacts becomes more difficult with increasing crater degradation. Impact craters and their associated ejecta deposits obscure the underlying material, making plains unit identification difficult in certain situations; these impacts could have superposed either smooth or intercrater plains deposits. Therefore for Fig. 7 we mapped only the uppermost surface unit.

4.3.1.2. Smooth plains. Analysis of MESSENGER data has not substantially changed the definition of the smooth plains deposits from the original unit definition developed by the M10 team. Smooth plains are level to gently sloped over distances of 100–200 km, and they have a low density of superposed craters (e.g., Trask and Guest, 1975; Denevi et al., 2013a). These deposits can be expansive, such as the Caloris exterior plains (e.g., Trask and Guest, 1975; Denevi et al., 2013a) and the northern smooth plains (Head et al., 2011), and they can be small in area, contained within craters tens of kilometers in diameter. Smooth plains of volcanic origin are characterized by regionally smooth deposits; the presence of kipukas; sharp and distinctive color boundaries; an association with volcanic vents; the presence of partially buried impact craters, ghost craters, and wrinkle ridges at expected rim and peak ring locations; and burial of crater terraces by smooth plains (e.g., Head et al., 2008, 2009a, 2011; Denevi et al., 2013a).

4.3.1.3. Intercrater plains. The intercrater plains constitute a morphologic unit that can still be characterized by an extremely textured surface, caused by the high density of craters <10 km in diameter (Fig. 8). The areas mapped are plains regions between craters >20 km in diameter; the elevation of areas of intercrater plains varies by ~5 km, but the slope of the mapped plains regions is generally <2.0°. Thus, locally the intercrater plains are nearly level deposits, but regionally the plains are a more gently rolling or undulating unit. As mapped, the intercrater plains include a wide variety of heavily cratered surface morphologies, from regions with fresh and distinct secondary impact craters (Fig. 8a) to regions with muted surface textures where the secondary craters are degraded and have merged together (Fig. 8b–e). Secondary craters and chains tend to be in distributions radial to their primary crater (Fig. 8a and c).

4.3.2. Application to geologic mapping

On the basis of these definitions of plains units, the geological map in Fig. 7 was constructed. The mapped area (13.5×10^6 km^2) spans a substantial part of the western hemisphere of Mercury (80°N to 30°S and 180°E to 270°E). The map includes 7 of 10 of our study regions, in order to compare with previous geologic maps and to ensure that map patterns are not controlled by impact basin structures or long-wavelength topography that may have postdated plains formation (Zuber et al., 2012). The most current global tectonic maps (e.g., Byrne et al., 2014) indicate no major long-wavelength topographic undulations in our mapped region. The fractional areas occupied by the three units defined above are ~30% smooth plains, ~33% intercrater plains, and ~33% crater materials. The remaining area (~4%) is covered by hummocky Caloris interior units (Caloris Montes, Nervo Formation, and the Odin Formation) that do not meet the unit definitions described above and were therefore not mapped in this study.

The location of the map region to the east of Caloris is responsible for the nearly equivalent proportions of intercrater and smooth plains (Fig. 7). There is a high concentration of smooth plains deposits at 170°E longitude, within and around the Caloris basin, compared with other regions of Mercury (Denevi et al., 2013a). Approximately 78% of the mapped smooth plains area is contained in 15 large continuous deposits >15,000 km^2 in area; the remaining 23% of the smooth plains area (Fig. 7) consists of small (<15,000 km^2) deposits located within and adjacent to craters 20–200 km in diameter. The smooth plains deposits generally collocate with topographic lows; these areas are typically, but not exclusively, associated with impact structures.

All of the study areas previously mapped as intercrater plains on the basis of M10 data (Fig. 3) are still classified as intercrater plains in this map, except for ICP5. In contrast, the M10-defined intermediate plains (Fig. 6) are all reclassified because of our revision of unit definitions. Of the three intermediate plains study areas contained in the map (Fig. 7), one has been reclassified as entirely smooth plains (IP1), another is mostly intercrater plains material (IP2), and the last is dominated by smooth plains material (IP4).

4.4. Implications of geologic mapping

The region selected for mapping (Figs. 1 and 7) provides insights into the dominant formation process of the intercrater plains. The improved resolution and coverage of MESSENGER MDIS data have permitted detailed analysis of the additive effect of secondary craters on smooth plains. Secondary crater fields are extensive and can heavily modify the surface proximal to the impact crater. Young, volcanically emplaced smooth plains, such as the northern smooth plains (Head et al., 2011), can quickly develop an intercrater plains-like texture if there are multiple near-contemporaneous impacts within a small area (Fig. 9). This evolution from a smooth-plains to an intercrater-plains morphology can occur with as few as two young, nearby impact craters. For instance, the overlapping ejecta deposits of Gaudí and Stieglitz craters (Fig. 9a) create an intercrater plains texture (Fig. 9b) on part of the volcanically emplaced northern smooth plains. When the full region is assessed it is obvious that the area shown in Fig. 9b is a recently modified part of a larger smooth plains deposit.

This same effect is observed at larger scales as well (Fig. 9c and d). The northwestern boundary of Sobkou Planitia has been altered by Strindberg and Ahmad Baba craters (Fig. 9c). Intercrater plains and the smooth plains in this area have a gradational contact.

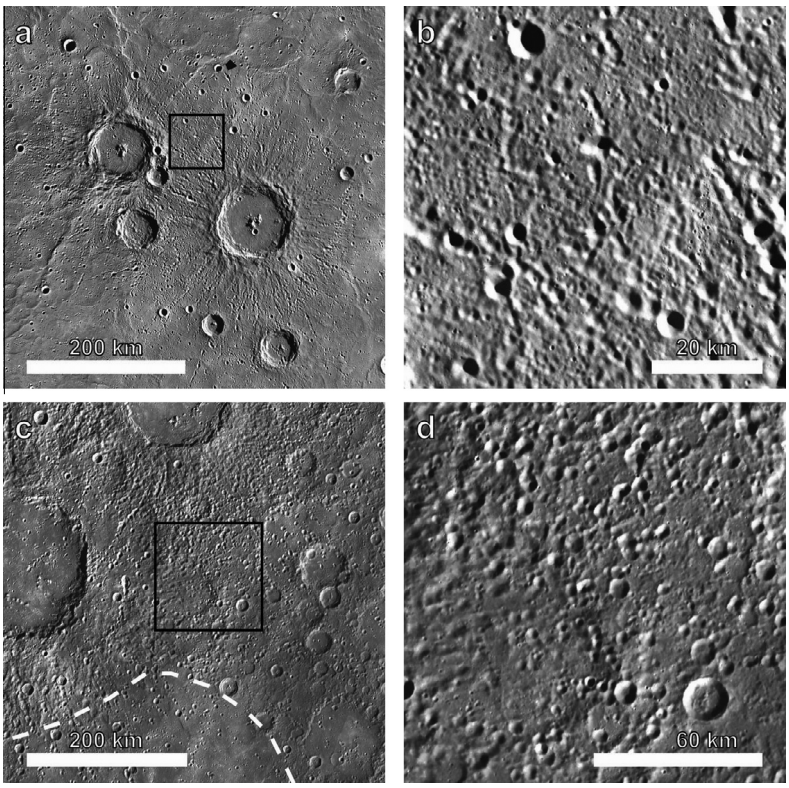

Fig. 9. Two examples of the transformation of smooth plains to intercrater plains by secondary cratering. (a) An area of northern smooth plains (Head et al., 2011) that includes the relatively young craters Gaudí (81 km diameter, left) and Stieglitz (100 km diameter, right). Black box outlines the area of panel (b). (b) Close-up of the overlapping ejecta deposits from Gaudí and Stieglitz craters. The overlapping secondary craters from Gaudí and Stieglitz created intercrater plains out of the northern smooth plains at this small scale. (c) An area surrounding two fresh impact craters, Strindberg (189 km diameter, left) and Ahmad Baba (126 km diameter, top), in the northwestern region of Sobkou Planitia, a basin-hosted smooth plains deposit. Superposition of ejecta deposits from the large craters has created an extensive intercrater plains deposit. The white dashed line shows the approximate boundary between the smooth and intercrater plains regions, and the black box outlines the area of panel (d). (d) An intercrater plains deposit created from the overlapping ejecta deposits of Strindberg and Ahmad Baba craters. These regions of intercrater plains (b and d) were created from the modification of smooth plains by the superposed ejecta deposits of only two craters each, emphasizing the rapidity with which intercrater plains can be formed.

The intercrater plains dominate in the northern portion of Fig. 9c and then eventually grade into smooth plains in the south. As in the area in Figs. 9a and b, the superposition of secondary craters from relatively young impact craters was able to produce intercrater plains from smooth plains.

It is easy to identify a buildup of secondary craters on extensive volcanic surfaces (e.g., 9a and b), but it becomes more difficult to map out crater materials when an impact occurs on a heavily cratered surface, such as the intercrater plains, because secondary crater fields can readily blend into the surrounding terrain. The two examples of Fig. 9 suggest that smooth volcanic plains could have formed throughout the geologic history of Mercury and later been heavily modified by nearby impact craters. During the early history of Mercury, when cratering rates were relatively high (e.g., Strom and Neukum, 1988; Marchi et al., 2009, 2013; Le Feuvre and Wieczorek, 2008), it would have been possible to convert a deposit of smooth volcanic plains into intercrater plains within a geologically short interval, making the identification of ancient volcanic deposits challenging from modern images.

That intercrater plains are typically found on gently undulating terrain is consistent with a volcanic origin. Typically, clearly identified smooth plains deposits on Mercury (e.g., Denevi et al., 2013a) are areally extensive, with gently rolling to level surfaces. Some such surfaces, however, have been modified by long-wavelength topographic change (e.g., Zuber et al., 2012; Klimczak et al., 2013; Byrne et al., 2014). The topographic signature associated with impact-produced deposits, such as the lunar Imbrian plains, in contrast, is more variable in that elevations do not cluster around a single elevation as they would with a more nearly horizontal original surface (Schultz and Spudis, 1979). However, the intercrater plains texture is observed both on the flanks of high-standing plateaus and in topographic depressions across the surface of Mercury (e.g., ICP4, ICP5, IP3). This observation suggests that the intercrater plains formation process must be able to act over an elevation range of several kilometers (a finding that would support an origin by emplacement of impact ejecta onto topography more nearly similar to that found today), or that the plains formed horizontal surfaces (a finding that would support an origin either as volcanic deposits or fluidized ejecta) that were subsequently modified by uplift, subsidence, or tilting (Oberst et al., 2010; Zuber et al., 2012; Klimczak et al., 2013) and secondary cratering.

Predicted extents of continuous ejecta deposits on Mercury (Gault et al., 1975; Melosh, 1989) suggest that the influence of the ejecta deposit does not extend outward of the crater rim by more than two crater radii, less than on the Moon because of Mercury's higher surface gravitational acceleration. By this rule of thumb, intercrater plains are observed to be more widely distributed than the lateral extent of continuous basin ejecta deposits and thus cannot all be impact-produced deposits (cf. Wilhelms, 1976). Analysis of the distribution of high-reflectance smooth plains around the lunar Orientale basin has shown that the majority of smooth plains occur at approximately two to four basin radii outward of the Cordillera Ring (Meyer et al., 2013). These observations support the idea that secondary basin ejecta materials should be considered as candidate source material for intercrater plains,

but it is important to keep in mind the differences (i.e., surface gravitational acceleration, impact velocity, target rheology) between the Moon and Mercury that could affect cratering efficiency on these two planetary bodies. The higher gravitational acceleration at the surface of Mercury is believed to have a substantial influence on the lower total extent of ejecta deposits compared with the Moon (e.g., Gault et al., 1975). Therefore, on Mercury, basin secondary ejecta deposits are likely to pond in terrain nearer to the basin rim than 2–4 basin radii. Even if basin secondary ejecta proves to be a substantial component (~20%; Meyer et al., 2013) of the material at 1.3–2.6 basin radii (scaling the lunar values by 0.65; Gault et al., 1975), the deposits formed are typically small and discontinuous, making it difficult to resurface large portions of the mercurian crust. Small, well-preserved basins such as Raditladi (258 km in diameter) and Rachmaninoff (306 km in diameter) do not have areally extensive plains deposits associated with their ejecta deposits. In addition, if discrete plains deposits did form on Mercury in this manner, then such deposits should be observed around young basins on Mercury similar in age to the lunar Orientale basin (~3.7 Ga; Le Feuvre and Wieczorek, 2011). Such deposits are not observed around young basins such as Rembrandt (Whitten et al., 2014).

A comparison of the distribution of intercrater plains on Mercury with the asymmetric distribution of known impact basins (Fassett et al., 2012) supports the interpretation that the formation mechanism for intercrater plains could be dominated by volcanic processes. However, at least a portion of the intercrater plains areas in this study are within approximately one basin radius of the nearest identified impact basin structure, indicating that basin ejecta is present at these sites, at least as a component of an impact-gardened regolith that also includes locally derived material (e.g., Oberbeck et al., 1974). For either plains emplacement mechanism, the number of craters with diameters >20 km (~7390 craters; Fassett et al., 2011) has been sufficient to produce the morphology (i.e., the rough texture produced by secondary impacts) observed across intercrater plains today.

A comparison of the crater density values and the smooth morphology of individual study regions lends support to the idea that volcanic activity on Mercury was widespread early in the planet's history (Fig. 5). From our analysis, an $N(10)$ value of ~225 can be used to distinguish between smooth and intercrater plains deposits. On the other hand, $N(20)$ crater density values have more overlap for regions that are morphologically classified as either smooth or intercrater plains. For example, IP3 and IP4 have high $N(20)$ values, suggesting that these regions are pre-Tolstojan in age. However, the MDIS color data and the dominant smooth morphology of IP3 and IP4 indicate that these are regions of smooth plains. This apparent contradiction can be resolved by an extended interval of eruptions of smooth plains lavas. The large $N(20)$ values, which include embayed craters in IP3 and IP4, represent the crater density on an ancient surface by this argument, whereas the $N(10)$ values record the age of the younger smooth plains. Craters >20 km in diameter are less likely to be buried by a volcanic eruption, having crater rim heights of ~0.66 km or more (Pike, 1988), and, therefore, can remain intact and observable even though the surrounding terrain and smaller craters are buried (e.g., Whitten and Head, 2013b). Craters <10 km in diameter, in contrast, have rim heights of <0.5 km (Pike, 1988), implying that lava flows at least 0.5 km thick would bury these smaller craters. This relationship between crater density and regional morphology is consistent with the view that early smooth plains on Mercury were emplaced volcanically and able to resurface the regions between large craters across large areas (Whitten and Head, 2013b). The variation in $N(10)$ for the identified smooth plains regions (i.e., ICP5, IP1, IP3, IP4, IP5) suggests variability in ages, an observation likely to be the result of differences in time of emplacement.

The spread in crater size–frequency distributions (Fig. 4) may not span the entire duration of volcanic activity and, instead, part of this variation may be the result of a variable preservation state of the intercrater plains deposits. Intercrater plains regions more heavily modified by volcanic resurfacing or basin ejecta deposition might have a lower crater density than well-preserved deposits and contribute to a spread in crater size–frequency distributions. Estimates of the timing of intercrater plains formation can be made by examining the crater size–frequency distributions for each of the study regions. Crater statistics for all of the regions defined as intercrater plains in our analysis (i.e., ICP1, ICP2, ICP3, ICP4, IP2) cluster together (Fig. 4k) and have $N(20)$ values of ~70–160 (Table 1). Whereas the crater size–frequency distributions are similar among the intercrater plains study regions, the cratering statistics are not identical, suggesting some variability in the unit ages. One recent estimate for the absolute age of a region with the highest observed crater density on Mercury is ~4.0–4.1 Ga (Marchi et al., 2013), providing evidence that ancient terrains can be preserved for billions of years on Mercury.

On the basis of the evidence outlined above, especially the rate at which smooth volcanic plains can be transformed into intercrater plains, we conclude that the intercrater plains could have formed as a series of areally extensive volcanic flows that were modified by superposed primary and secondary impacts. Stratigraphic relationships between the intercrater plains and superposed impact craters suggest that this unit was deposited over an extended period of time during the period of heavy bombardment, an inference supported by crater size–frequency distributions (Fig. 5, Table 1). This interpretation of intercrater plains formation differs from the proposal that such units were emplaced largely as impact deposits (e.g., Wilhelms, 1976; Oberbeck et al., 1977). The continual emplacement of volcanic flows and subsequent modification would result in a continuum of cratered deposits; the oldest deposits are the most densely cratered and highly textured (Fig. 8e) whereas the youngest plains deposits have an abundance of secondary craters but are not as modified as the older deposits (Fig. 8a). Other evidence presented in previous studies, including a paucity of craters <100 km diameter (e.g., Strom, 1977; Strom et al., 2011; Fassett et al., 2011) and the near-global distribution of the intercrater plains (Trask and Guest, 1975; Spudis and Prosser, 1984; Denevi et al., 2009; Fig. 7), supports the interpretation that the intercrater plains were formed by the modification of early volcanic deposits during the period of heavy bombardment.

More data are needed to fully understand the origin of the intercrater plains unit. Since much of the surface of Mercury has been affected by impact processes it would be helpful to know the composition of the material excavated by craters tens of kilometers in diameter superposed on the mapped intercrater plains to determine the composition at depth (e.g., Denevi et al., 2013b). If the excavated compositions of these craters are similar to the HRP/IP color unit typical of the smooth plains or if the crater material has compositions distinct from the surrounding terrain, such information would provide strong evidence for a volcanic origin. If the excavated materials have a compositional signature similar to that of the impacted surface, such information would lend more support to an impact-related formation hypothesis. High-resolution spectral datasets from MESSENGER's Mercury Atmospheric and Surface Composition Spectrometer (MASCS) (McClintock and Lankton, 2007) and the MErcury Radiometer and Thermal Infrared Spectrometer (MERTIS) instrument (Hiesinger et al., 2010) on the BepiColombo Mercury Planetary Orbiter (Benkhoff et al., 2010) can be utilized to identify mineralogically distinct intercrater plains regolith by employing spectral classification (e.g., D'Amore et al., 2013; Izenberg et al., 2014) or spectral mixing models. Analysis of global topography, particularly with regional slopes

removed (e.g., Head et al., 2002), would aid in analyzing elevation across the intercrater plains by highlighting variations that might be typical of volcanic flooding (e.g., Whitten and Head, 2013b). Lastly, a high-resolution global topographic dataset, especially at lower latitudes where intercrater plains are mapped, would enable analysis of the surface roughness of all intercrater plains regions, potentially enabling identification of subunits (e.g., Kreslavsky and Head, 2000; Kreslavsky et al., 2013; Yang et al., 2013).

5. Conclusions

High-resolution MESSENGER data acquired at optimal viewing geometries for morphologic mapping studies have enabled a more detailed analysis of the intercrater and intermediate plains units defined for Mercury's surface during the mapping and data analysis that followed the Mariner 10 flybys. The lower resolution of M10 images and lack of systematic topographic measurements caused some features (e.g., crater and basin rims, degraded and subdued craters) to be included in "plains." MESSENGER datasets indicate that the plains units are most easily identified and mapped on the basis of morphology and areal density of impact craters. Intercrater plains are highly textured, sculpted by impact ejecta, and covered with secondary craters in a variety of states of degradation. Crater size–frequency distributions indicate that the intercrater plains are ancient and are consistently older than the smooth plains. MDIS color data indicate that the intercrater plains are characterized by a wide variety of spectral units. From this analysis, we interpret the intermediate plains to be composed mainly of intercrater plains with patches of smooth plains material and, therefore, we suggest that the intermediate plains unit should be subdivided into these two units and that each should then be mapped separately. The removal of the intermediate plains makes the distinction between the smooth plains and the intercrater plains clearer than in earlier maps and analyses.

Our work supports a volcanic origin for a substantial percentage of the intercrater plains (Fig. 7). The basis for this conclusion includes (1) the ability of ejecta from a small number of superposed craters to transform known smooth plains deposits of volcanic origin into a unit indistinguishable from intercrater plains; (2) the variety of ancient ages for intercrater plains deposits as interpreted from crater size–frequency distributions; and (3) the near-global distribution of intercrater plains (between craters $\geqslant$30 km in diameter) compared with the uneven distribution of impact basins and their associated ejecta deposits. Several conditions early in Mercury's history also support a volcanic origin for intercrater plains including the lack of a low-density anorthositic crust (Nittler et al., 2011), the extended distribution of younger volcanic deposits (e.g., Denevi et al., 2013a), and the paucity of craters <100 km diameter (e.g., Strom, 1977; Fassett et al., 2011; Marchi et al., 2013).

Nonetheless, an impact origin is still a possibility for some intercrater plains. For example, MESSENGER data have revealed several local intercrater plains deposits that are interpreted to be impact related (Denevi et al., 2013b). These case studies indicate the importance of interpreting each individual deposit with care and seeking characteristics (Table 2) that would support either a volcanic or impact-related origin.

Despite the difficulty in ascertaining the origin of a specific occurrence of intercrater plains, this work provides useful criteria for distinguishing the different plains units on Mercury. The unit definitions described in this study, especially for the intercrater plains, can be used to produce consistent geological maps of Mercury and aid in the interpretation of specific examples of intercrater plains. Additionally, spectral information from MASCS, elemental information from MESSENGER's GRS and X-Ray Spectrometer, and data from the future BepiColombo mission (e.g., the MERTIS instrument) can be used to further define unit boundaries and identify mineralogically or compositionally distinct intercrater plains material. An ability to identify and map the distribution of more rigorously defined intercrater and smooth plains will aid in unraveling the geological stratigraphy of Mercury. Once the intercrater plains have been fully mapped, subtle variations in morphology, spectral properties, and topography can be investigated to define deposits of varying age and, more broadly, sharpen our understanding of the geologic history of Mercury.

Acknowledgments

We gratefully acknowledge funding from the MESSENGER project, which is supported by the NASA Discovery Program under contracts NASW-00002 to the Carnegie Institution of Washington and NAS5-97271 to The Johns Hopkins University Applied Physics Laboratory.

References

Antonenko, I., Head, J.W., Mustard, J.F., Hawke, B.R., 1995. Criteria for the detection of lunar cryptomaria. Earth Moon Planets 69, 141–172.
Becker, K.J. et al., 2012. Global controlled mosaic of Mercury from MESSENGER orbital images. Lunar Planet. Sci. 43. Abstract 2654.
Benkhoff, J. et al., 2010. BepiColombo – Comprehensive exploration of Mercury: Mission overview and science goals. Planet. Space Sci. 58, 2–20. http://dx.doi.org/10.1016/j.pss.2009.09.020.
Byrne, P.K. et al., 2013. An assemblage of lava flow features on Mercury. J. Geophys. Res. Planets 118, 1303–1322. http://dx.doi.org/10.1002/jgre.20052.
Byrne, P.K., Klimczak, C., Şengör, A.M.C., Solomon, S.C., Watters, T.R., Hauck II, S.A., 2014. Mercury's global contraction much greater than earlier estimates. Nat. Geosci. 7, 301–307. http://dx.doi.org/10.1038/NGE02097.
Cavanaugh, J.F. et al., 2007. The Mercury Laser Altimeter instrument for the MESSENGER mission. Space Sci. Rev. 131, 451–479. http://dx.doi.org/10.1007/s11214-007-9273-4.
Cintala, M.J., 1992. Impact-induced thermal effects in the lunar and Mercurian regoliths. J. Geophys. Res. 97, 947–973. http://dx.doi.org/10.1029/91JE02207.
Crater Analysis Techniques Working Group, 1979. Standard techniques for presentation and analysis of crater size–frequency data. Icarus 37, 467–474.
Cruikshank, D.P., Hartmann, W.K., Wood, C.A., 1973. Moon: 'Ghost' craters formed during mare filling. Moon 7, 440–452.
D'Amore, M. et al., 2013. Exploiting the Mercury surface reflectance spectroscopy dataset from MESSENGER: Making sense of three million spectra. Lunar Planet. Sci. 44. Abstract 1900.
DeHon, R.A., Scott, D.H., Underwood, J.R., 1981. Geologic map of the Kuiper (H-6) Quadrangle of Mercury. Map I-1233, Misc. Investigations Ser., U.S. Geological Survey, Denver, Colo.
Denevi, B.W. et al., 2009. The evolution of Mercury's crust: A global perspective from MESSENGER. Science 324, 613–618. http://dx.doi.org/10.1126/science.1172226.
Denevi, B.W. et al., 2013a. The distribution and origin of smooth plains on Mercury. J. Geophys. Res. Planets 118, 891–907. http://dx.doi.org/10.1002/jgre.20075.
Denevi, B.W. et al., 2013b. The volcanic origin of a region of intercrater plains. Lunar Planet. Sci. 44. Abstract 1218.
Edmundson, K.L. et al., 2011. Preliminary photogrammetric control of MESSENGER orbital images of Mercury. Abstracts with Programs 43 (5), Paper 100-6. Geological Society of America, Boulder, Colo., p. 267.
Eggleton, R.E., Schaber, G.G., 1972. Cayley formation interpreted as basin ejecta. In: Apollo 16 Preliminary Science Report. Special Publication SP-315, NASA, Washington, DC, pp. 29-7 to 29-16.
Fassett, C.I. et al., 2009. Caloris impact basin: Exterior geomorphology, stratigraphy, morphometry, radial sculpture, and smooth plains deposits. Earth Planet. Sci. Lett. 285, 297–308. http://dx.doi.org/10.1016/j.epsl.2009.05.022.
Fassett, C.I., Kadish, S.J., Head, J.W., Solomon, S.C., Strom, R.G., 2011. The global population of large craters on Mercury and comparison with the Moon. Geophys. Res. Lett. 38, L10202. http://dx.doi.org/10.1029/2011GL047294.
Fassett, C.I. et al., 2012. Large impact basins on Mercury: Global distribution, characteristics, and modification history from MESSENGER orbital data. J. Geophys. Res. 117, E00L08. http://dx.doi.org/10.1029/2012JE004154.
Freed, A.M. et al., 2012. On the origin of graben and ridges within and near volcanically buried craters and basins in Mercury's northern plains. J. Geophys. Res. 117, E00L06. http://dx.doi.org/10.1029/2012JE004119.
Gast, P.W. et al., 1973. The Apollo 16 lunar samples: Petrographic and chemical description. Science 179, 23–34.
Gault, D.E., Guest, J.E., Murray, J.B., Dzurisin, D., Malin, M.C., 1975. Some comparisons of impact craters on Mercury and the Moon. J. Geophys. Res. 80, 2444–2460.

Grolier, M.J., Boyce, J.M., 1984. Geologic map of the Borealis region (H-1) of Mercury. Map I-1660, Misc. Investigations Ser., U.S. Geological Survey, Denver, Colo.
Guest, J.E., Fielder, G., 1968. Lunar ring structures and the nature of the maria. Planet. Space Sci. 16, 665–673.
Guest, J.E., Greeley, R., 1983. Geologic map of the Shakespeare (H-3) Quadrangle of Mercury. Map I-1408, Misc. Investigations Ser., U.S. Geological Survey, Denver, Colo.
Hapke, B., Danielson, G.E., Klaasen, K., Wilson, L., 1975. Photometry and colorimetry of Mercury. J. Geophys. Res. 80, 2431–2443.
Hawke, B.R., Spudis, P.D., 1980. Geochemical anomalies on the eastern limb and farside of the Moon. In: Papike, J.J., Merrill, R.B. (Eds.), Proceedings of the Conference on the Lunar Highlands Crust. Pergamon, New York, pp. 467–481.
Hawkins III, S.E. et al., 2007. The Mercury Dual Imaging System on the MESSENGER spacecraft. Space Sci. Rev. 131, 247–338. http://dx.doi.org/10.1007/s11214-007-9266-3.
Head, J.W., 1974. Stratigraphy of the Descartes region (Apollo 16): Implications for the origin of samples. Moon 11, 77–99.
Head, J.W., Solomon, S.C., 1981. Tectonic evolution of the terrestrial planets. Science 213, 62–76.
Head, J.W., Wilson, L., 1992. Lunar mare volcanism: Stratigraphy, eruption conditions, and the evolution of secondary crusts. Geochim. Cosmochim. Acta 56, 2155–2175. http://dx.doi.org/10.1016/0016-7037(92)90183-J.
Head, J.W., Kreslavksy, M.A., Pratt, S., 2002. Northern lowlands of Mars: Evidence for widespread volcanic flooding and tectonic deformation in the Hesperian Period. J. Geophys. Res. 107 (E1), 5003. http://dx.doi.org/10.1029/2000JE001445.
Head, J.W. et al., 2008. Volcanism on Mercury: Evidence from the first MESSENGER flyby. Science 321, 69–72. http://dx.doi.org/10.1126/science.1159256.
Head, J.W. et al., 2009a. Volcanism on Mercury: Evidence from the first MESSENGER flyby for extrusive and explosive activity and the volcanic origin of plains. Earth Planet. Sci. Lett. 285, 222–242. http://dx.doi.org/10.1016/j.epsl.2009.03.007.
Head, J.W. et al., 2009b. Evidence for intrusive activity on Mercury from the first MESSENGER flyby. Earth Planet. Sci. Lett. 285, 251–262. http://dx.doi.org/10.1016/j.epsl.2009.03.008.
Head, J.W. et al., 2011. Flood volcanism in the northern high latitudes of Mercury revealed by MESSENGER. Science 333, 1853–1856. http://dx.doi.org/10.1126/science.1211997.
Hiesinger, H., Helbert, J., MERTIS Co-I Team, 2010. The Mercury Radiometer and Thermal Infrared Spectrometer (MERTIS) for the BepiColombo mission. Planet. Space Sci. 58, 144–165. http://dx.doi.org/10.1016/j.pss.2008.09.019.
Hodges, C.A., Muehlberger, W.R., Ulrich, G.E., 1973. Geologic setting of Apollo 16. Proc. Lunar Sci. Conf. 4, 1–25.
Hurwitz, D.M. et al., 2013. Investigating the origin of candidate lava channels on Mercury with MESSENGER data: Theory and observations. J. Geophys. Res. Planets 118, 471–486. http://dx.doi.org/10.1029/2012JE004103.
Izenberg, N.R., Klima, R.L., Murchie, S.L., Blewett, D.T., Holsclaw, G.M., McClintock, W.E., Malaret, E., Mauceri, C., Vilas, F., Sprague, A.L., Helbert, J., Domingue, D.L., Head III, J.W., Goudge, T.A., Solomon, S.C., Hibbitts, C.A., Dyar, M.D., 2014. The low-iron, reduced surface of Mercury as seen in spectral reflectance by MESSENGER. Icarus 228, 364–374.
Kiefer, W.S., Murray, B.C., 1987. The formation of Mercury's smooth plains. Icarus 72, 477–491.
King, J.S., Scott, D.H., 1990. Geologic map of the Beethoven (H-7) Quadrangle of Mercury. Map I-2048, Misc. Investigations Ser., U.S. Geological Survey, Denver, Colo.
Klimczak, C. et al., 2013. Insights into the subsurface structure of the Caloris basin, Mercury, from assessments of mechanical layering and changes in long-wavelength topography. J. Geophys. Res. Planets 118, 2030–2044. http://dx.doi.org/10.1002/jgre.20157.
Kreslavsky, M.A., Head, J.W., 2000. Kilometer-scale roughness of Mars: Results from MOLA data analysis. J. Geophys. Res. 105, 2669526711. http://dx.doi.org/10.1029/2000JE001259.
Kreslavsky, M.A., Head, J.W., Neumann, G.A., Rosenburg, M.A., Aharonson, O., Smith, D.E., Zuber, M.T., 2013. Lunar topographic roughness maps from Lunar Orbiter Laser Altimeter (LOLA) data: Scale dependence and correlation with geologic features and units. Icarus 226, 52–66. http://dx.doi.org/10.1016/j.icarus.2013.04.027.
Le Feuvre, M., Wieczorek, M.A., 2008. Nonuniform cratering of the terrestrial planets. Icarus 197, 291–306. http://dx.doi.org/10.1016/j.icarus.2008.04.011.
Le Feuvre, M., Wieczorek, M.A., 2011. Nonuniform cratering of the Moon and a revised crater chronology of the inner Solar System. Icarus 214, 1–20. http://dx.doi.org/10.1016/j.icarus.2011.03.010.
Leake, M.A., 1981. The Intercrater Plains of Mercury and the Moon: Their Nature, Origin, and Role in Terrestrial Planet Evolution. Ph.D. Thesis, Univ. Arizona, Tucson, Ariz.
Marchi, S., Mottola, S., Cremonese, G., Massironi, M., Martellato, E., 2009. A new chronology for the Moon and Mercury. Astron. J. 137, 4936–4948. http://dx.doi.org/10.1088/0004-6256/137/6/4936.
Marchi, S., Chapman, C.R., Fassett, C.I., Head, J.W., Bottke, W.F., Strom, R.G., 2013. Global resurfacing of Mercury 4.0–4.1 billion years ago by heavy bombardment and volcanism. Nature 499, 59–61. http://dx.doi.org/10.1038/nature12280.
McClintock, W.E., Lankton, M.R., 2007. The Mercury Atmospheric and Surface Composition Spectrometer for the MESSENGER mission. Space Sci. Rev. 131, 481–521. http://dx.doi.org/10.1007/s11214-007-9264-5.
McGill, G.E., King, E.A., 1983. Geologic map of the Victoria (H-2) Quadrangle of Mercury. Map I-1409, Misc. Investigations Ser., U.S. Geological Survey, Denver, Colo.
Melosh, H.J., 1989. Impact Cratering: A Geologic Process. Oxford Univ. Press, Oxford, UK, 245pp.
Meyer, H.M., Denevi, B.W., Boyd, A.K., Robinson, M.S., 2013. The distribution and origin of lunar light plains around Orientale basin. Lunar Planet Sci. 44. Abstract 1539.
Milton, D.J., 1964. Stratigraphy of the Terra Part of the Theophilus Quadrangle. Astrogeol. Studies Ann. Prog. Rept., July 1963 to July 1964, pt. A, Open-file Report, U.S. Geological Survey, Denver, Colo., pp. 17–27.
Muehlberger, W.R., Hörz, F., Sevier, J.R., Ulrich, G.E., 1980. Mission objectives for geological exploration of the Apollo 16 landing site. In: Papike, J.J., Merrill, R.B. (Eds.), Proceedings of the Conference on the Lunar Highlands Crust. Pergamon, New York, pp. 1–49.
Murray, B.C. et al., 1974. Mercury's surface: Preliminary description and interpretation from Mariner 10 pictures. Science 185, 169–179. http://dx.doi.org/10.1126/science.185.4146.169.
Murray, B.C., Strom, R.G., Trask, N.J., Gault, D.E., 1975. Surface history of Mercury: Implications for terrestrial planets. J. Geophys. Res. 80, 2508–2514. http://dx.doi.org/10.1029/JB080i017p02508.
Nittler, L.R. et al., 2011. The major-element composition of Mercury's surface from MESSENGER X-ray spectrometry. Science 333, 1847–1850. http://dx.doi.org/10.1126/science.1211567.
Oberbeck, V.R., Morrison, R.H., Hörz, F., Quaide, W.L., Gault, D.E., 1974. Smooth plains and continuous deposits of craters and basins. Proc. Lunar Sci. Conf. 5, 111–136.
Oberbeck, V.R., Quaide, W.L., Arvidson, R.E., Aggarwal, H.R., 1977. Comparative studies of lunar, martian, and mercurian craters and plains. J. Geophys. Res. 82, 1681–1698.
Oberst, J., Preusker, F., Phillips, R.J., Watters, T.R., Head, J.W., Zuber, M.T., Solomon, S.C., 2010. The morphology of Mercury's Caloris basin as seen in MESSENGER stereo topographic models. Icarus 209, 230238. http://dx.doi.org/10.1016/j.icarus.2010.03.009.
O'Keefe, J.D., Ahrens, T.J., 1977. Impact-induced energy partitioning, melting, and vaporization on terrestrial planets. Proc. Lunar Planet. Sci. Conf. 8, 3357–3374.
Peplowski, P.N. et al., 2011. Radioactive elements on Mercury's surface from MESSENGER: Implications for the planet's formation and evolution. Science 333, 1850–1852. http://dx.doi.org/10.1126/science.1211576.
Pike, R.J., 1988. Geomorphology of impact craters on Mercury. In: Vilas, F., Chapman, C.R., Matthews, M.S. (Eds.), Mercury. Univ. Ariz. Press, Tucson, Ariz., pp. 165–273.
Rava, B., Hapke, B., 1987. An analysis of the Mariner 10 color ratio map of Mercury. Icarus 71, 397–429. http://dx.doi.org/10.1016/0019-1035(87)90037-6.
Richardson, J.E., 2009. Cratering saturation and equilibrium: A new model looks at an old problem. Icarus 204, 697–715.
Robinson, M.S., Lucey, P.G., 1997. Recalibrated Mariner 10 color mosaics: Implications for mercurian volcanism. Science 275, 197–200. http://dx.doi.org/10.1126/science.275.5297.197.
Robinson, M.S. et al., 2008. Reflectance and color variations on Mercury: Regolith processes and compositional heterogeneity. Science 321, 66–69.
Schaber, G.G., McCauley, J.F., 1980. Geologic map of the Tolstoj (H-8) Quadrangle of Mercury. Map I-1199, Misc. Investigations Ser., U.S. Geological Survey, Denver, Colo.
Schultz, P.H., Spudis, P.D., 1979. Evidence for ancient mare volcanism. Proc. Lunar Planet. Sci. Conf. 10, 2899–2918.
Shearer, C.K. et al., 2006. Thermal and magmatic evolution of the Moon. Rev. Mineral. Geochem. 60, 365–518.
Spudis, P.D., Guest, J.E., 1988. Stratigraphy and geologic history of Mercury. In: Vilas, F., Chapman, C.R., Matthews, M.S. (Eds.), Mercury. Univ. Ariz. Press, Tucson, Ariz., pp. 118–164.
Spudis, P.D., Prosser, J.G., 1984. Geologic map of the Michaelangelo (H-12) Quadrangle of Mercury. Map I-1659, Misc. Investigations Ser., U.S. Geological Survey, Denver, Colo.
Strom, R.G., 1977. Origin and relative age of lunar and mercurian intercrater plains. Phys. Earth Planet. Inter. 15, 156–172.
Strom, R.G., Neukum, G., 1988. The cratering record on Mercury and the origin of impacting objects. In: Vilas, F., Chapman, C.R., Matthews, M.S. (Eds.), Mercury. Univ. Ariz. Press, Tucson, Ariz., pp. 336–373.
Strom, R.G., Trask, N.J., Guest, J.E., 1975. Tectonism and volcanism on Mercury. J. Geophys. Res. 80, 2478–2507.
Strom, R.G., Malin, M.C., Leake, M.A., 1990. Geologic map of the Bach (H-15) Quadrangle of Mercury. Map I-2015, Misc. Investigations Ser., U.S. Geological Survey, Denver, Colo.
Strom, R.G., Chapman, C.R., Merline, W.J., Solomon, S.C., Head, J.W., 2008. Mercury cratering record viewed from MESSENGER's first flyby. Science 321, 79–81. http://dx.doi.org/10.1126/science.1159317.
Strom, R.G. et al., 2011. Mercury crater statistics from MESSENGER flybys: Implications for stratigraphy and resurfacing history. Planet. Space Sci. 59, 1960–1967. http://dx.doi.org/10.1016/j.pss.2011.03.018.
Taylor, S.R., 1989. Growth of planetary crusts. Tectonophysics 161, 147–156.
Trask, N.J., 1976. Cratering history of the heavily cratered terrain on Mercury. Geol. Romana 15, 471–476.
Trask, N.J., Dzurisin, D., 1984. Geologic map of the Discovery (H-11) Quadrangle of Mercury. Map I-1658, Misc. Investigations Ser., U.S. Geological Survey, Denver, Colo.

Trask, N.J., Guest, J.E., 1975. Preliminary geologic terrain map of Mercury. J. Geophys. Res. 80, 2461–2477. http://dx.doi.org/10.1029/JB080i017p02461.
Watters, T.R., 1993. Compressional tectonism on Mars. J. Geophys. Res. 98, 17049–17060. http://dx.doi.org/10.1029/93JE01138.
Watters, T.R. et al., 2012. Extension and contraction within volcanically buried impact craters and basins on Mercury. Geology 40, 1123–1126.
Whitten, J.L., Head, J.W., 2013a. Ancient lunar mare volcanism: Identification, distribution, and composition of cryptomare deposits. Lunar Planet. Sci. 44. Abstract 1247.
Whitten, J.L., Head, J.W., 2013b. Detecting volcanic resurfacing of heavily cratered terrain: Flooding simulations on the Moon using Lunar Orbiter Laser Altimeter (LOLA) data. Planet. Space Sci. 85, 24–37. http://dx.doi.org/10.1016/j.pss.2013.05.013.
Whitten, J.L., Head, J.W., Helbert, J., Solomon, S.C., 2014. Rembrandt basin: Distinguishing between volcanic and impact-produced smooth plains deposits on Mercury. Lunar Planet. Sci. 45. Abstract 1289.
Wilhelms, D.E., 1976. Mercurian volcanism questioned. Icarus 28, 551–558. http://dx.doi.org/10.1016/0019-1035(76)90128-7.
Wilhelms, D.E., McCauley, J., 1971. Geological map of the near side of the Moon. Map I-703. Misc. Investigations Ser., U.S. Geological Survey, Denver, Colo.
Wilson, L., Head, J.W., 2008. Volcanism on Mercury: A new model for the history of magma ascent and eruption. Geophys. Res. Lett. 35, L23205. http://dx.doi.org/10.1029/2008GL035620.
Xiao, Z., Strom, R.G., Chapman, C.R., Head, J.W., Klimczak, C., Ostrach, L.R., Helbert, J., D'Incecco, P., 2014. Comparisons of fresh complex impact craters on Mercury and the Moon: Implications for controlling factors in impact crater excavation. Icarus 228, 260–275.
Yang, D., Zuber, M.T., Head, J.W., Solomon, S.C., 2013. Distribution of topographic slope and roughness in Mercury's northern hemisphere. Lunar Planet. Sci. 44. Abstract 2347.
Young, J.W., Mattingly, T.K., Duke, C.M., 1972. Crew observations. In: Apollo 16 Preliminary Science Report. Special Publication SP-315, NASA, Washington, DC, pp. 5-1 to 5-6.
Zuber, M.T. et al., 2012. Topography of the northern hemisphere of Mercury from MESSENGER laser altimetry. Science 336, 217–220. http://dx.doi.org/10.1126/science.1218805.